JOURNAL OF GEOPHYSICAL RESEARCH: OCEANS, VOL. 118, 2547–2564, doi:10.1002/jgrc.20181, 2013

Southern Ocean nutrient trapping and the efficiency of the biological pump

François W. Primeau,[1] Mark Holzer,[2,3] and Timothy DeVries[4]

Received 21 July 2012; revised 15 January 2013; accepted 27 March 2013; published 21 May 2013.

[1] We present a data-assimilated model of the ocean's phosphorus cycle that is constrained by climatological phosphate, temperature, salinity, sea-surface height, surface heat and freshwater fluxes, as well as chlorofluorocarbon-11(CFC-11) and natural $\Delta^{14}C$. Export production is estimated to be $5.8 \pm 2.0 \times 10^{12}$ mol P/yr of which (26 ± 6)% originates in the Southern Ocean (SO) south of 40°S. The biological pump efficiency, defined as the proportion of the ocean's phosphate inventory that is regenerated, is (39 ± 7)%. Dividing the SO south of 40°S into a sub-Antarctic zone (SANTZ) and an Antarctic zone (ANTZ) separated by the latitude of maximum Ekman divergence, we estimate that the SANTZ and ANTZ account, respectively, for (23 ± 5)% and (3 ± 1)% of global export production, (17 ± 4)% and (3 ± 1)% of the regenerated nutrient inventory, and (31 ± 1)% and (43 ± 5)% of the preformed nutrient inventory. Idealized SO nutrient depletion experiments reveal a large-scale transfer of nutrients into circumpolar and deep waters and from the preformed to the regenerated pool. In accord with the concept of the biogeochemical divide, we find that nutrient drawdown in the ANTZ is more effective than in the SANTZ for increasing the efficiency of the biological pump, while having a smaller impact on production in regions north of 40°S. Complete SO nutrient drawdown would allow the biological pump to operate at 94% efficiency by short circuiting the transport of nutrients in northward Ekman currents, leading to a trapping of nutrients in circumpolar and deep waters that would decrease production outside the SO by approximately 44% while increasing it in the SO by more than 725%.

Citation: Primeau, F. W., M. Holzer, and T. DeVries (2013), Southern Ocean nutrient trapping and the efficiency of the biological pump, *J. Geophys. Res. Oceans*, *118*, 2547–2564, doi:10.1002/jgrc.20181.

1. Introduction

[2] The Southern Ocean (SO) ventilates a large fraction of the ocean, both through the formation of newly ventilated water masses and through the exposure to the atmosphere of old water masses [*Toggweiler and Samuels*, 1993; *Primeau*, 2005; *Primeau and Holzer*, 2006; *DeVries and Primeau*, 2011]. This fact, combined with some of the largest surface nutrient concentrations in the world, causes the SO to be a large "leak" in the ocean's biological pump: The exposure to the atmosphere of old water masses allows respired CO_2 to escape to the atmosphere while the downward transport of preformed nutrients into the ocean interior represents a "missed opportunity" for the biota in the surface ocean to drawdown CO_2 and sequester it in the thermocline and deep ocean [*Sigman et al*., 2010].

[3] Three-dimensional ocean general circulation model (GCM) simulations of SO nutrient drawdown have demonstrated that increasing biological production and nutrient drawdown in the SO would greatly increase the strength of the biological pump, but they have also shown that biological production in the rest of the ocean tends to decrease with increased nutrient depletion in the SO [*Sarmiento and Orr*, 1991; *Sarmiento et al*., 2004; *Marinov et al*., 2006; *Oschlies et al*., 2010]. *Sarmiento et al*. [2004] used silicic acid data in conjunction with a GCM to show that a considerable fraction of the export production north of 30°S is maintained by nutrients originating from the SO. Consistent with these findings, *Dutkiewicz et al*. [2005] demonstrated that the biological productivity of the subtropical gyres is coupled to the degree of iron limitation in the SO. By increasing atmospheric iron deposition into the SO in their model, they showed that the increase in SO production is accompanied by decreased lateral transport of phosphate and decreased production in the subtropical gyres.

[1]Department of Earth System Science, University of California, Irvine, California, USA.
[2]Department of Applied Mathematics, School of Mathematics and Statistics, University of New South Wales, New South Wales, Australia.
[3]Also at Department of Applied Physics and Applied Mathematics, Columbia University, New York City, New York, USA.
[4]Department of Atmospheric and Oceanic Sciences, University of California, Los Angeles, CA, USA.

Corresponding author: F. W Primeau, Department of Earth System Science, University of California, Irvine, Croul Hall, Irvine, CA 92697, USA. (fprimeau@uci.edu)

2169-9275/13/10.1002/jgrc.20181

[4] *DeVries et al*. [2012] coupled a data-assimilated ocean circulation model to a simple phosphorus cycling model in which biological production was parameterized as being proportional to the concentration of phosphate in the euphotic layer, with no spatial variations in the proportionality (rate) constant, and conducted a sequence of simulations in which they varied the rate constant for the biological phosphate uptake. Their idealized experiments showed that SO export production increased dramatically as the rate constant increased. Although they did not specifically make the point, their result also showed that in the subtropics biological production started to decrease once the rate constant was increased from $(5\ \text{years})^{-1}$ to $(2\ \text{years})^{-1}$. That biological production can decrease even when the production rate constant increases points to a large-scale redistribution of nutrients associated with changes in biological production, enriching some regions while depleting others. In the study by *DeVries et al*. [2012], the focus was on characterizing regional differences in sequestration efficiency, that is, on differences in the time that regenerated organic matter remains in the ocean interior before being reexposed to the surface. Therefore, that publication did not document the interior redistribution of nutrients accompanying changes in export production. Here we explore in more detail how changes in production couple to transport by sinking particles and the large-scale circulation to trap nutrients in the SO and as a result decrease nutrient availability in the rest of the ocean. A key novel aspect of our study is that in comparison to previous studies [e.g., *Sarmiento and Orr*, 1991; *Sarmiento et al*., 2004; *Marinov et al*., 2006], we use a much better steady-state circulation estimate that has been constrained by observations. In addition, our formulation of the phosphorus cycling model affords novel, numerically efficient diagnostics of the preformed and regenerated phosphate pools, of which nutrients were last in the euphotic zone, and a rigorous quantification of export production.

[5] Our goal is to answer the following questions:

[6] (1) What is the three-dimensional distribution of preformed and regenerated nutrients in the ocean, and how do these distributions change when SO biological production increases?

[7] (2) How does the SO influence the efficiency of the biological pump? What proportion of the preformed and regenerated phosphate inventories originate in the SO, and how do these proportions change as biological production changes in the SO?

[8] (3) How does export production outside the SO change in response to more efficient biological phosphate uptake in the SO?

[9] To answer these questions, we develop a simple linear phosphorus cycling model, which we combine with a dynamical ocean circulation model and observations to simultaneously estimate biological production and ocean circulation on global scales. The resulting data-assimilated model allows us to infer large-scale patterns of biological production from the signature of uptake, particle transport, and remineralization imprinted on the large-scale phosphate field of the 2009 World Ocean Atlas (WOA) [*Garcia et al*., 2010a]. We also formulate new diagnostic equations that allow us to quantify sources and distributions of preformed and regenerated nutrients in the ocean. The diagnostics take advantage of the assumption of linearity used in the formulation of our model to partition the phosphate field according to where its preformed part was last in contact with the surface and according to where its regenerated part was last exported from the euphotic layer in either dissolved or particulate organic form. We then use our optimized circulation model to systematically perturb SO production in the spirit of the numerical experiments by *Sarmiento and Orr* [1991], *Sarmiento et al*. [2004], and *Marinov et al*. [2006] to quantify how nutrients become trapped in the SO, depleting their concentration elsewhere, and how the efficiency of the biological pump is affected by this trapping. The patterns of the teleconnection of worldwide production with SO productivity, and paths and timescales with which these teleconnections are mediated, are explored in a separate publication [*Holzer and Primeau*, 2012].

2. Data-Assimilated Circulation and Phosphate Cycling Model

[10] We use the model and data-assimilation technique described by *DeVries and Primeau* [2011], with several improvements, the most important being a doubling of the model's horizontal resolution to $2^\circ \times 2^\circ$ and the addition of CFC-11 and PO_4 data to the list of observational constraints previously assimilated by the model (temperature, salinity, sea-surface height, surface heat and fresh water fluxes, as well as natural $\Delta^{14}C$). In addition to using the National Centers for Environmental Prediction (NCEP) heat and freshwater fluxes as constraints in the objective function, the model's momentum equations are forced using the NCEP wind-stress climatology [*Trenberth et al*., 1989].

[11] The objective function has the same general form as in the study of *DeVries and Primeau* [2011], except that we have added the following terms here:

$$C_{F_{11}} = \left(\boldsymbol{H}_F F_{11} - F_{11}^{\text{obs}}\right)^T \Gamma_{F_{11}}^{-1} \left(\boldsymbol{H}_F F_{11} - F_{11}^{\text{obs}}\right), \tag{1}$$

$$C_{\text{PO}_4} = \left(\boldsymbol{H}_P P_I - P_I^{\text{obs}}\right)^T \Gamma_P^{-1} \left(\boldsymbol{H}_P P_I - P_I^{\text{obs}}\right), \tag{2}$$

and

$$C_J = J^T \Gamma_J^{-1} J. \tag{3}$$

[12] In (1)–(3), P_I is the equilibrium phosphate (PO_4) distribution and F_{11} is the simulated transient CFC-11 concentration; $\Gamma_{F_{11}}$ and Γ_P are the error covariance matrices for CFC-11 and PO_4, and Γ_J is the covariance matrix for the prior probability distribution of the biological phosphate uptake rate per unit volume, J. The quantity Γ_J^{-1} takes the form of a horizontal Laplacian operator subject to zero-flux boundary conditions at the basin boundaries. Its effect is to assign a lower prior probability to J fields with excessive small scale variations. To ensure that J can never be negative, we use the logarithm of J instead of J itself as the control parameter while minimizing the objective function. The matrix $\boldsymbol{H}_F$ subsamples the F_{11} state vector to years and grid boxes for which CFC-11 observations are available in the Global Data Analysis Project database [*Key et al*., 2004]. Similarly, $\boldsymbol{H}_P$ subsamples P_I to the grid boxes of phosphate data in the 2009 WOA [*Garcia et al*., 2010b].

[13] In addition to adding a vector of discretized log J values to the list of control parameters, we have also added the global mean phosphate concentration $\overline{P}_I$ and the exponent b of the Martin curve as a control parameter (see section 3 for more details on the phosphorus cycling model to be optimized). Unlike *Schlitzer* [2002, 2004] and *Schlitzer et al*. [2004], but like *Kwon and Primeau* [2006], for simplicity we did not allow the value of b to vary spatially.

[14] At the numerically determined minimum of the objective function, all of its terms are of order unity. The contributions to the objective function from temperature and salinity are $C_\theta = (1.3)^2$ and $C_S = (0.8)^2$, which corresponds to root-mean-squared deviations of 0.64°C and 0.092 practical salinity units (psu). Not surprisingly, given that the model has no seasonal cycle, the largest temperature misfits are in the seasonal thermocline. For the top 355 m of the water column, the root-mean-squared deviation reaches 1.65°C. However, in spite of these upper-ocean temperature errors, the model's zonally averaged pycnocline depth, as defined by *Gnanadesikan et al*. [2002], $D \equiv -\int_{z_{\rm bot}}^{0} (\rho - \rho_{\rm max}) z \mathrm{d}z / \int_{z_{\rm bot}}^{0} (\rho - \rho_{\rm max}) \mathrm{d}z$, closely matches the value computed from the annually averaged 2009 WOA with a root-mean-squared deviation of ~29 m, which corresponds to an average relative error of ~12%.

[15] The contribution to the objective function from the PO_4, CFC-11, and $\Delta^{14}C$ constraints are $C_{PO_4} = (0.69)^2$, $C_{F_{11}} = (1.0)^2$, and $C_{14_C} = (0.72)^2$. The C_J smoothing cost contribution was negligible compared to the C_{PO_4} contribution, suggesting that the phosphate observations do not provide a strong constraint on the small-scale features of the biological production field. However, the phosphate distribution combined with dynamical information does constrain the large-scale open-ocean biological uptake and export of phosphate.

[16] Figure 1 summarizes the quality of our data-assimilated circulation model in terms of the fidelity of its passive tracer fields. It shows the joint cumulative distribution functions for the observed and modeled phosphate, CFC-11, and radiocarbon concentrations. The joint distribution was estimated using the kernel density estimation method described in *Botev et al*. [2010], which we modified to include a grid-box-volume weights. Figure 1 shows a joint distribution that is tightly clustered along the 1:1 line, demonstrating that the model's tracer transport produces fields closely matched to observations, which suggests that the model's phosphate cycle and biological production should also closely match those of the real ocean. However, we hasten to point out that while the transport estimates from our data-assimilated model are of much higher fidelity than those from forward models, they are not uniquely constrained and substantial uncertainty remains, especially because of the relatively coarse resolution of our model and because of the lack of an explicitly resolved seasonal cycle.

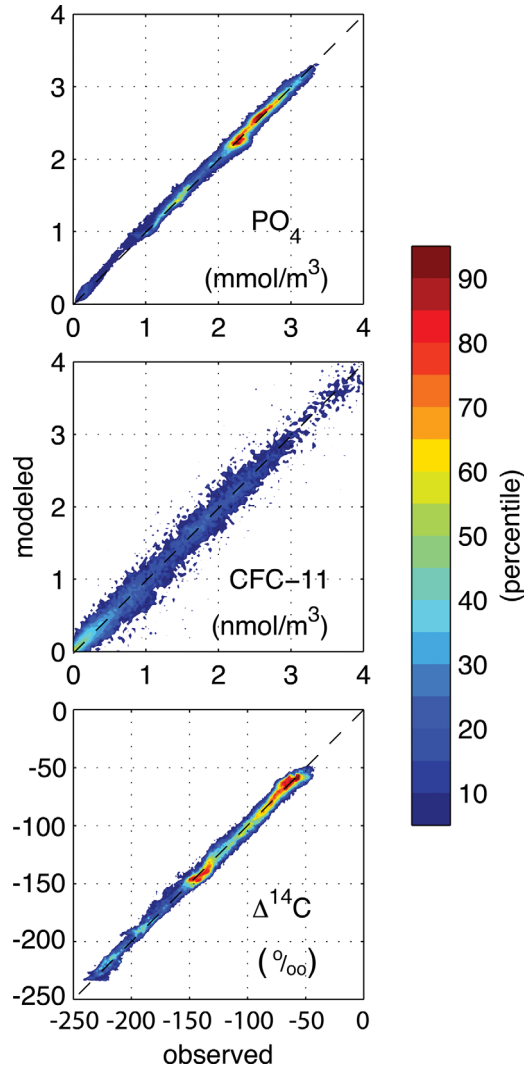

Figure 1. Joint distribution function for the gridbox-volume-weighted observed and modeled tracer concentrations expressed in terms of the percentiles of the cumulative distribution function. The Nth percentile is defined such that N% of the joint distribution lies outside N% contour. Contours with large percentiles correspond to the highest density and cluster close to the 1:1 line.

3. A Linear Phosphate Cycling Model

[17] We consider two pools of phosphorus: an inorganic pool (phosphate, PO_4) and a semilabile organic pool (dissolved organic phosphorus (DOP)), whose concentrations are denoted, respectively, by P_I and P_O. All biological production first converts PO_4 to DOP before remineralizing back into phosphate with a rate constant, $\kappa = (0.5\text{years})^{-1}$. A fraction $\sigma = 1/3$ of the production is assigned to P_O locally, while a fraction $1 - \sigma$ is exported to depth following a power-law particle-flux profile [*Martin et al*., 1987] with exponent $b = 0.70$, a value that was determined as part of the data assimilation. Our optimized b value is smaller than the value of $b = 0.856$ obtained from sediment-trap data by *Martin et al*. [1987], but nearly equal to the value obtained from a more extensive sediment-trap data set by *Primeau* [2006] ($b = 0.70$). Our value is also significantly smaller than the average value obtained by *Schlitzer* [2002] ($b = 1.04$) and *DeVries et al*. [2012] ($b = 0.82$), using similar data-assimilation approaches but for different phosphorus cycling models and objective functions. A smaller power-law exponent b implies that particulate organic matter remineralizes deeper in the water

column. Because semilabile DOP remineralizes predominantly in the upper water column, the larger value of the power-law exponent b obtained in the study of *DeVries et al*. [2012] might in part be explained as a compensation for the absence of DOP in their phosphorus cycling model. For our model, the DOP concentration ranges from 0.06 ± 0.04 μmol/kg in the surface layer to less than 0.001 ± 0.004 μmol/kg for depths below 215 m. (See also section 4.2 and Figure 12 for the zonally averaged pattern of DOP concentration.) For comparison, *Abell et al*. [2000] report values of DOP for the North Pacific between 0.1 and 0.3 μmol/kg at the surface to near zero by 200 m. The DOP concentration in our model is significantly lower than observed, but it does not include labile DOP that cycles on timescales of hours to months, nor does it include semirecalcitrant DOP that cycles on timescales of years or longer. (The sensitivity of the total, preformed, and regenerated phosphate distribution to changes in the phosphorus cycle model parameters, including the exponent b, is shown in Appendix A).

[18] The governing equation for the phosphorus fields is

$$\frac{\mathrm{d}}{\mathrm{d}t}\begin{bmatrix} P_I \\ P_O \end{bmatrix} + \begin{bmatrix} \mathcal{T} + \gamma(\mathbf{r}) & -\kappa \\ -\mathcal{S} & \mathcal{T} + \kappa \end{bmatrix}\begin{bmatrix} P_I \\ P_O \end{bmatrix} = \begin{bmatrix} 0 \\ 0 \end{bmatrix}, \tag{4}$$

where $\gamma(\mathbf{r})$ is the spatially varying rate "constant" for the biological uptake of phosphate, $\mathcal{T} \equiv \nabla \cdot [\mathbf{u} - \mathbf{K} \cdot \nabla]$ is the advection-diffusion transport operator subject to no-flux boundary conditions at the surface and on the basin boundaries, and $\mathcal{S}$ is a linear operator that combines the biological production of organic phosphorus with the sinking particle transport of organic phosphorus, i.e.,

$$\mathcal{S}P_I \equiv \begin{cases} \sigma\gamma P_I & \text{if} \quad z \geq z_c, \\ (1-\sigma)\left[\dfrac{\partial}{\partial z}\left(\Theta(z-z_b)\left(\dfrac{z}{z_c}\right)^{-b}\right)\right]\displaystyle\int_{z_c}^{0} \gamma P_I \mathrm{d}z & \text{if} \quad z < z_c. \end{cases} \tag{5}$$

[19] Here $z_c = -73.4$ m is the base of the euphotic layer, i.e., the vertical coordinate of the bottom of the model's second layer; $\Theta(z - z_b)$ is a Heaviside step function that ensures conservation of phosphorus by forcing the particle flux reaching the ocean bottom at $z = z_b$ to be allocated to P_O. The local phosphate uptake rate constant is determined as $\gamma(\mathbf{r}) = J(\mathbf{r})/P_I(\mathbf{r})$. The resulting spatial variations in the value of γ parameterize differences in biological production due to light intensity, grazing pressure, and the availability of nutrients other than phosphate. Note that $\gamma(\mathbf{r})$ is identically equal to zero in the aphotic zone $(z < z_c)$.

[20] Equations (4) and (5) are discretized into n grid boxes using second-order finite differences and recast into matrix form to take advantage of MATLAB's sparse matrix functionality, which allows the model and its diagnostic equations to be coded and solved efficiently. The fields $P_I(\mathbf{r}), P_O(\mathbf{r})$, and $\gamma(\mathbf{r})$ become n-dimensional column vectors, with the row index indicating position, $\mathbf{r}$. The operators $\mathcal{T}$ and $\mathcal{S}$ become sparse $n \times n$ matrices $\mathbf{T}$ and $\mathbf{S}$, respectively. Because the $\mathcal{T}$ and $\mathcal{S}$ are discretized using a scheme that preserves the flux-divergence nature of the operators, the model conserves the total phosphorus mass.

[21] For a given total mass of phosphorus, the model's equilibrium state can be obtained by time stepping the model forward in time until transients die out. However, a computationally much more efficient alternative to time stepping is to set the time derivative to zero and then solve the resulting system of linear algebraic equations by direct matrix inversion [*Kwon and Primeau*, 2006, 2008]. Because the initial condition does not enter into this second approach, the constraint on the total mass of phosphorus is imposed using a weak "geological" restoring term [e.g., *Li and Primeau*, 2008] to the steady-state version of equation (4), so that P_I is restored to the optimized global mean of $\overline{P}_I = 2.1769$ mmol/m^3, with a timescale, $1/\gamma_g = 10^6$ years, that is sufficiently long compared to the longest eigen-timescale of $\mathbf{T}$ to ensure that the asymptotic long-time solution to the initial value problem is practically identical to the solution obtained by direct matrix inversion.

[22] Defining the diagonal matrices, $\boldsymbol{\gamma} = \mathbf{diag}(\gamma(\mathbf{r}))$ and $\boldsymbol{\gamma}_g = \gamma_g \mathbf{I}$, where $\mathbf{I}$ is the $n \times n$ identity matrix, the linear system governing the equilibrium state is

$$\begin{bmatrix} \mathbf{T} + \boldsymbol{\gamma} + \boldsymbol{\gamma}_g & -\kappa\mathbf{I} \\ -\mathbf{S} & \mathbf{T} + \kappa\mathbf{I} \end{bmatrix}\begin{bmatrix} P_I \\ P_O \end{bmatrix} = \begin{bmatrix} \gamma_g \overline{P}_I \\ 0 \end{bmatrix}. \tag{6}$$

[23] Note that the geological restoring term has been split into $\gamma_g P_I$ inside the matrix and $\gamma_g \overline{P}_I$ on the right-hand side. Equation (6) is solved by sparse LU factorization followed by back substitution. The geological restoring term, being extremely small, is neglected in all diagnostic expressions presented below.

4. Data-Assimilated Base State

4.1. Biological Export Production

[24] The biological production $J = \gamma P_I$ in the linear phosphate-cycling model is neither net primary production (NPP) nor export production. NPP includes the production that rapidly recycles locally without affecting the large-scale distribution of phosphate. This part of the NPP is therefore unconstrained by the observed phosphate distribution used to infer production in our data-assimilated model. More important for large-scale nutrient cycling and better constrained by our assimilation model is the export production—the part of the production that remineralizes below the euphotic zone. However, because J includes the production of semilabile organic matter, which partly regenerates in the euphotic zone, we cannot equate it with export production. One possibility is to subtract the remineralization rate of organic matter to obtain what is referred to as new production [*Gnanadesikan et al*., 2002]:

$$J_{\mathrm{new}} = \gamma P_I - \kappa P_O, \tag{7}$$

for locations in the euphotic zone. For a one-dimensional model in steady state, export production equals new production, but for a three-dimensional model with lateral transport of organic matter, this is not the case. As far as we know, export production has never been diagnosed accurately in a model that includes the lateral transport of dissolved organic matter.

[25] To accurately diagnose our model's equilibrium export production, we must determine the part of the production that will eventually remineralize below the euphotic

zone. We accomplish this by partitioning P_O according to the horizontal grid box where the organic matter was produced and then integrating the remineralization rate per unit volume of this organic matter over the aphotic zone, that is, we integrate the remineralization of DOP produced in a given grid box both vertically and horizontally over the entire volume of the ocean below the euphotic zone. Because our model satisfies the steady-state assumption, the integrated remineralization rate from a given grid box is equal to the export production from that grid box.

4.1.1. Diagnostic Equations for Export Production

[26] For the equilibrium state of our phosphate-cycling model, the concentration of organic matter at $\mathbf{r}$ that was produced in an infinitesimal volume element d^3r' at $\mathbf{r}'$ in the euphotic layer, $\mathcal{P}_O(\mathbf{r}|\mathbf{r}')d^3\mathbf{r}'$ obeys

$$[\mathcal{T}+\kappa]\mathcal{P}_O(\mathbf{r}|\mathbf{r}') = \mathcal{S}P_I(\mathbf{r}')\delta(\mathbf{r}-\mathbf{r}'), \tag{8}$$

subject to no-flux boundary conditions. The Dirac delta function on the right-hand side labels the phosphorus during uptake according to the point $\mathbf{r}'$ where the production occurs. Linearity allows us to recover the total DOP field by superposition,

$$P_O(\mathbf{r}) = \int \mathcal{P}_O(\mathbf{r}|\mathbf{r}')d^3r'. \tag{9}$$

Furthermore, the steady state allows us to equate the rate of export per unit volume from $\mathbf{r}'$ to the integrated aphotic-zone remineralization rate κP_O of $\mathbf{r}'$-labeled organic matter

$$J_{\text{ex}}(\mathbf{r}') = \int_\Omega d^3r\,\kappa\mathcal{P}_O(\mathbf{r}|\mathbf{r}'), \tag{10}$$

where the domain Ω is the aphotic zone.

[27] To calculate J_{ex} numerically, we discretize the equations, which then become in matrix form

$$[\mathbf{T}+\kappa\mathbf{I}]\mathbf{P}_O = \mathbf{S}\,\mathbf{diag}(P_I), \tag{11}$$

where $\mathbf{P}_O$ is the discrete analogue of $P_O(\mathbf{r}|\mathbf{r}')d^3r'$, which is an $n\times n$ matrix, whose column index identifies the discretized source coordinate $\mathbf{r}'$ and whose row index identifies the discretized field coordinate $\mathbf{r}$. (Note that, equivalently, $\mathbf{P}_O\mathbf{W}^{-1}$ is the discrete analogue of $\mathcal{P}(\mathbf{r}|\mathbf{r}')$, where $\mathbf{W}$ is a diagonal matrix whose elements are the grid-box volumes.) Thus, the jth column of $\mathbf{P}_O$ is the discretized three-dimensional distribution of organic matter that was produced in the jth grid box, or equivalently, whose ith row is the partitioning of the organic matter in the ith grid box into n components according to the grid box where it was produced. (Only the columns corresponding to the n_s grid boxes in the euphotic layer are not identically zero.) The total DOP field is obtained by summing the columns of $\mathbf{P}_O$, i.e., $P_O = \mathbf{P}_O\mathbf{1}$, which is the discrete analogue of the superposition integral (9). The integral over $\mathbf{r}'$ in (10) is equivalent to integrating the columns of $\kappa\mathbf{P}_O$ over the volume of the ocean below the euphotic layer. To compute the integral, we introduce the mask vector Ω defined as a column vector whose elements are equal to zero for grid boxes in the euphotic layer and equal to one for the grid boxes below the euphotic layer. A volume integral over the domain below the euphotic layer is then equivalent to multiplying from the left by $\Omega^T\mathbf{W}$, so that the export production, J_{ex}, is given by

$$J_{\text{ex}}^T = \kappa\Omega^T\mathbf{W}\mathbf{P}_O\mathbf{W}^{-1}, \tag{12}$$

in which we have multiplied from the right by $\mathbf{W}^{-1}$ to divide the columns of $\mathbf{P}_O$ by the volume of the grid box at $\mathbf{r}'$, where the production occurred to obtain the export production rate per unit $\mathbf{r}'$ volume. Using equation (11) to eliminate $\mathbf{P}_O$ and taking the transpose yields

$$\begin{aligned} J_{\text{ex}} &= \kappa\,\mathbf{diag}(P_I)\,\mathbf{W}^{-1}\mathbf{S}^T[\mathbf{T}+\kappa\mathbf{I}]^{-T}\mathbf{W}\Omega \\ &\equiv \kappa\,\mathbf{diag}(P_I)\,\mathbf{S}^\dagger\,[\mathbf{T}^\dagger+\kappa\mathbf{I}]^{-1}\Omega, \end{aligned} \tag{13}$$

where $\mathbf{T}^\dagger \equiv \mathbf{W}^{-1}\mathbf{T}^T\mathbf{W}$ is the adjoint advection-diffusion transport operator and $\mathbf{S}^\dagger \equiv \mathbf{W}^{-1}\mathbf{S}^T\mathbf{W}$ is the adjoint production and particle transport operator. The advantage of the adjoint (i.e., transposed) formulation of equation (14) compared to equation (12) is that it computes J_{ex} by solving the equilibrium tracer distribution for a single tracer field with source $\Omega(\mathbf{r})$ as opposed to a separate solution for each grid box in the euphotic layer: the inverse of $\left[\mathbf{T}^\dagger+\kappa\mathbf{I}\right]$ is applied to a single column vector, Ω, as opposed to the n_s nonzero columns in $\mathbf{Sdiag}(P_I)$ on the right-hand side of equation (11).

4.1.1.1. Results

[28] The data-assimilated model's vertically integrated biological production is shown in Figure 2a. To make it easier to compare this estimate to other estimates of biological production, we converted our phosphate uptake rate, $J = \gamma P_I$, to carbon units using the Redfield C:P ratio of 106:1. Figure 2b shows the vertically and zonally integrated production J, export production J_{ex}, and new production, $J_{\text{new}} \equiv J - \kappa P_O$. On average, export production is approximately 30% lower than production itself, but with large-scale variations in the proportion of J that is exported. The zonally integrated J_{ex} varies between 60% of the zonally integrated J along the equator to nearly 80% near 50°S and 60°N. New production is generally very similar to export production, except in low latitudes where the lateral transport of P_O can be significant.

[29] Apart from the differences in magnitude, the large-scale open-ocean patterns of production are similar to the satellite-derived open-ocean annual NPP maps [e.g., *Sarmiento and Gruber*, 2006] with elevated production in the Arabian Sea and along the western coast of the Americas and Africa as well as in bands along the Equatorial Pacific and near 45°S and 45°N. Absent from the model production fields are the high coastal NPP values of the satellite-derived fields. This is due in part to the fact that we have zeroed biological production in waters less than two grid cells deep (i.e., shallower than the model's euphotic zone) to avoid unphysical nutrient trapping in coastal regions where the flow is not sufficiently resolved.

4.2. Remineralization Field

[30] Balancing the export production is the remineralization of organic matter below the euphotic zone. The phosphate remineralization (or "regeneration") rate is shown in Figure 3, expressed using the more familiar units of oxygen utilization

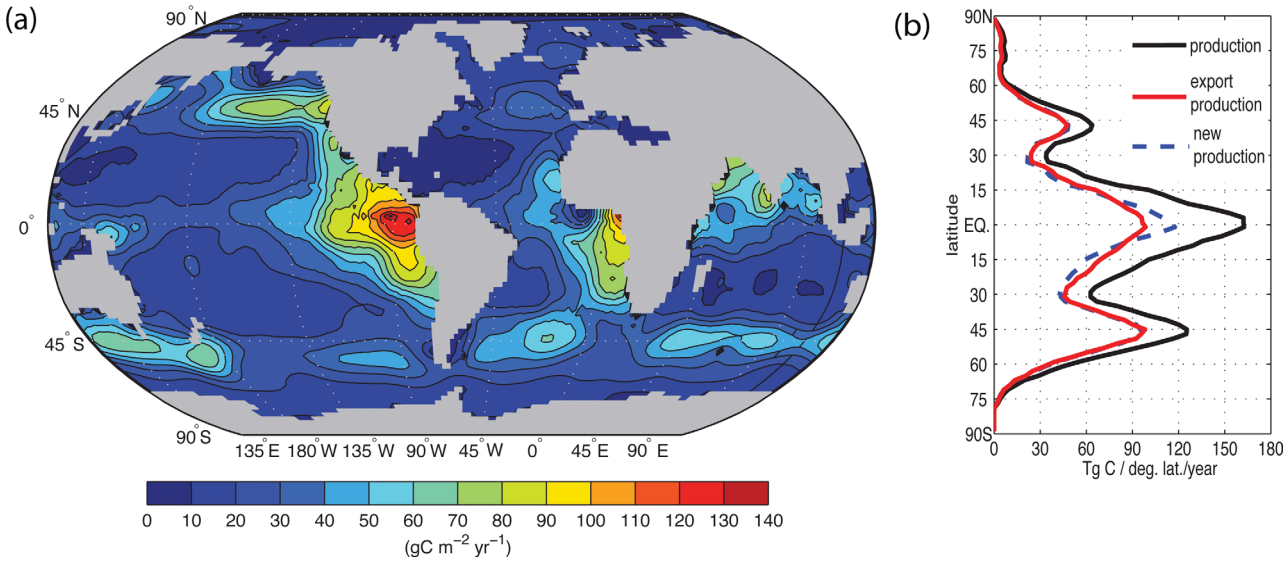

Figure 2. (a) Biological production expressed in units of g C/(m^2 yr) using a C:P ratio of 106. (b) Zonally integrated profiles of production (black), export production (red), new production (dashed blue), expressed in units of 10^{12} g C /(degree latitude year).

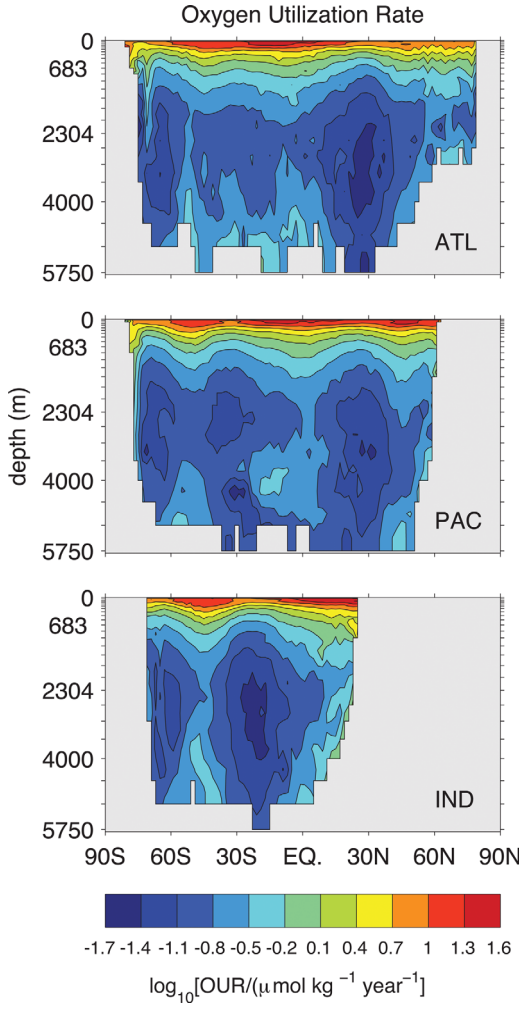

Figure 3. Zonally averaged OUR. The base-10 log of OUR/(1 μmol/(kg yr)) is contoured.

rate (OUR) (OUR $= R_{O_2:P}\kappa P_O$) and using a constant oxygen-to-phosphorus stoichiometric ratio of $R_{O_2:P} = 170$. Figure 3 shows that OUR decreases by about 2 orders of magnitude from the surface to a depth of ~1000 m. There are also significant meridional variations in the zonal average, with OUR varying by more than a factor of 2 or 3 along with the meridional structure of J_{ex} seen in Figure 2. Note that Figure 3 shows the logarithm of OUR. The contour range from 0.7 to 1.6 corresponds to a DOP concentration between 0.01 and 0.12 μmol/kg.

4.3. Preformed and Regenerated Phosphate Fields

[31] Partitioning the nutrient field into its preformed and regenerated parts is key to quantifying the efficiency of the biological pump [*Sigman and Boyle*, 2000; *Ito and Follows*, 2005]. The separation also sheds light on the cycling of nutrients in the real ocean and in models. Indeed, *Duteil et al*. [2012] have shown that models can produce reasonably good phosphate distributions, despite having large errors in the partition into preformed and regenerated components.

[32] Preformed phosphate, P_{pre}, is that part of the phosphate field that is carried into the interior from the euphotic zone (or surface) by water parcels. Regenerated phosphate, P_{reg}, is the part of the phosphate field that results from the remineralization of organic matter that is produced biologically at the surface and then carried into the interior in dissolved organic form by water parcels or by sinking particulate organic matter. Thus, by definition, all phosphate at the surface is preformed, and regenerated phosphate is reassigned to preformed phosphate as soon as it reenters the euphotic zone. The preformed and regenerated phosphate add up to total phosphate:

$$P_I = P_{pre} + P_{reg}. \tag{14}$$

[33] The separation into preformed and regenerated phosphate is usually based on the apparent oxygen utilization

Table 1. Globally Integrated Export Production, Regenerated Phosphate Inventory, and Preformed Phosphate Inventory Partitioned According to the Region of Ocean Where They Originated[a]

	Export Production	Regenerated Inventory	Preformed Inventory
Global	$5.8 \pm 2.0 \times 10^{12}$ mol P/yr	$1.1 \pm 0.2 \times 10^{15}$ mol P	$1.7 \pm 0.2 \times 10^{15}$ mol P
ANTZ	(3± 1)%	(3± 1)%	(43± 5)%
SANTZ	(23± 5)%	(17± 4)%	(31± 1)%
N. of 40°S	(74± 6)%	(80± 4)%	(25± 4)%

[a]The uncertainties, δZ, in the quantities, Z, presented in Table 1 were assigned based on the linear sensitivities to the phosphate cycle model parameters, b, σ, and κ, evaluated at the base equilibrium state as $(\delta Z)^2 = (\partial_b Z \delta b)^2 + (\partial_\sigma Z \delta\sigma)^2 + (\partial_\kappa Z \delta\kappa)^2$, where we took $\delta b = 0.35$, $\delta\sigma = 0.15$, and $\delta\kappa = (0.25\text{years})^{-1}$ as prior uncertainties for these parameters. See Appendix A for a parameter sensitivity analysis for b, σ, and κ.

(AOU), with the regenerated concentration given by $P_{\text{reg}} = \text{AOU}/R_{O_2:P}$, and the preformed part given by $P_{\text{pre}} = P_I - P_{\text{reg}}$ [*Ito and Follows*, 2005; *Duteil et al.*, 2012]. AOU is used as a matter of convenience because we generally do not know the ocean's advective-diffusive transport operator, which is needed to untangle how much of the phosphate field was transported preformed from the surface and how much was regenerated along the way. Here, we avoid using AOU by explicitly tracking preformed phosphate from the surface ocean into the interior using our data-assimilated transport operator [*DeVries et al.*, 2012]. This has the advantage of avoiding errors associated with uncertainties in $R_{O_2:P}$, in the degree to which the oxygen concentration of surface waters is in equilibrium with the atmosphere [*Ito et al.*, 2004], and with the substitution of nitrate as an oxidant in open-ocean oxygen minimum zones and in bottom sediments. The uncertainties associated with the operator approach stem from errors in the estimated advection-diffusion tracer transport operator, which we believe have been kept to a minimum by the observational constraints. Uncertainties aside, the main advantage of the operator approach is that we can further partition the preformed and regenerated phosphate according to their region of surface origin. This allows us to better identify which regions are the key contributors to preformed inventories, i.e., to indentify where the leaks in the biological pump are located.

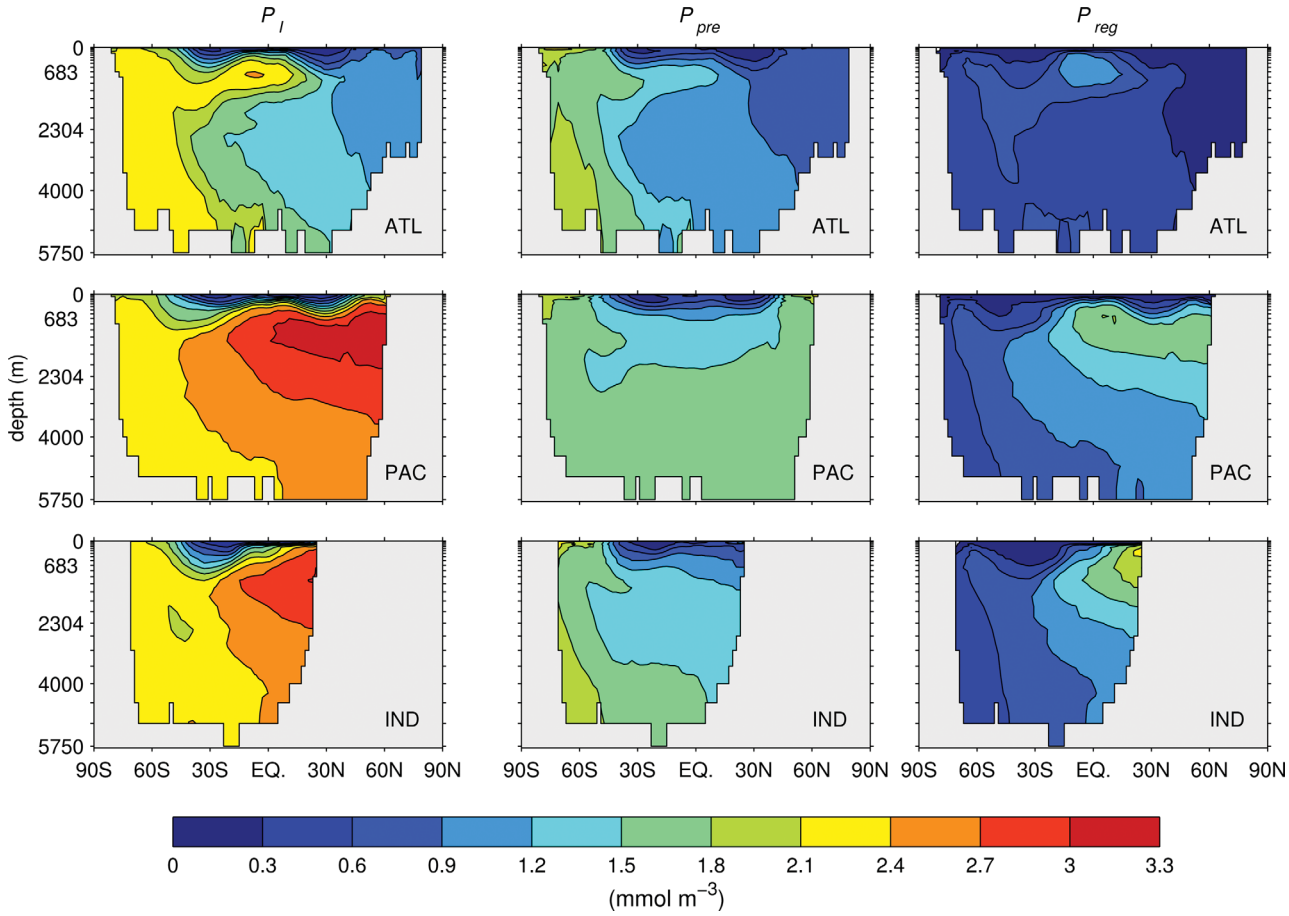

Figure 4. Zonally averaged phosphate concentration (P_I), preformed phosphate concentration (P_{pre}), and regenerated phosphate concentration (P_{reg}) in the Indian, Pacific, and Atlantic basins.

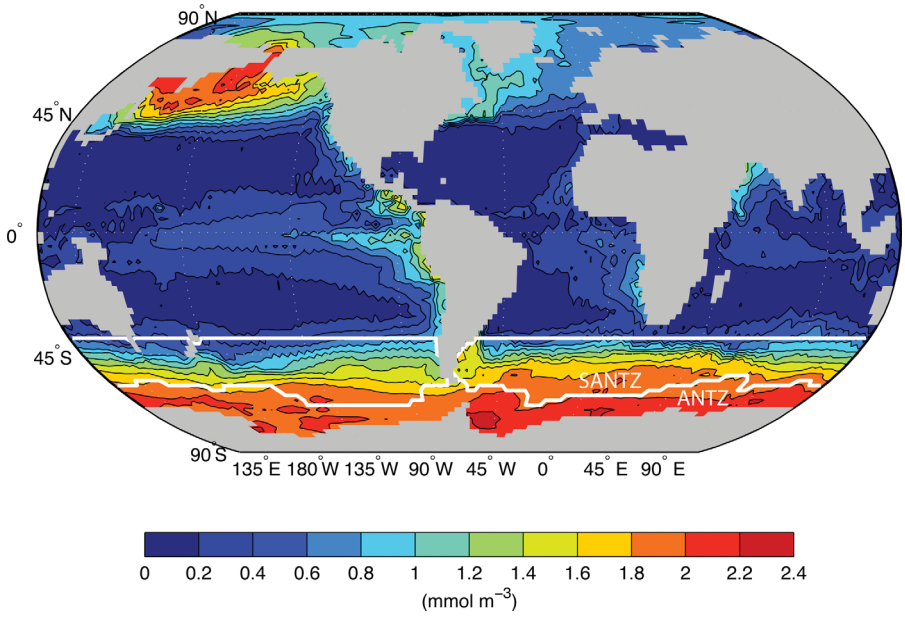

Figure 5. Average PO_4 concentration in the upper 73.4 m of the water column (model euphotic layer). The boundary separating the ANTZ and SANTZ as well as the northern boundary of the SANTZ at 40°S are indicated with thick white lines.

4.3.1. Diagnostic Equations for Preformed Phosphate

[34] The preformed component of phosphate can be computed by solving the ocean's advection-diffusion transport equation subject to a concentration surface boundary condition [e.g., *Primeau and Deleersnijder*, 2009; *DeVries et al.*, 2012], which prescribes the phosphate concentration at the surface to match the equilibrium solution of equation (6). For convenience, we impose this boundary condition by adding a near-instantaneous restoring term with a timescale $\tau_a = 1$s in the euphotic layer to essentially clamp P_{pre} to P_I in the euphotic layer. The resulting governing equation in continuous form is the partial differential equation

$$[\mathcal{T} + \gamma_a]\mathcal{P}_{\text{pre}}(\mathbf{r}|\mathbf{r}') = \gamma_a P_I(\mathbf{r})\delta(\mathbf{r} - \mathbf{r}'), \tag{15}$$

with $\gamma_a(\mathbf{r}) = 1/\tau_a$ in the euphotic zone and $\gamma_a = 0$ elsewhere. Equation (16) is solved subject to no-flux boundary conditions at all the basin boundaries including the sea surface. In (15), the quantity $\mathcal{P}_{\text{pre}}(\mathbf{r}|\mathbf{r}')d^3r'$ is the concentration of preformed phosphate at $\mathbf{r}$ that was last in contact with the euphotic layer in an infinitesimal volume d^3r' centered at $\mathbf{r}'$.

[35] The discretized equation corresponding to (15) is

$$[\mathbf{T} + \boldsymbol{\gamma}_a]\mathbf{P}_{\text{pre}} = \boldsymbol{\gamma}_a \mathbf{diag}(P_I), \tag{16}$$

where $\boldsymbol{\gamma}_a = \mathbf{diag}(\Omega^c)/\tau_a$ and $\Omega^c = 1 - \Omega$ is a mask vector for the euphotic zone. Here, $\mathbf{P}_{\text{pre}}$ is the discrete analogue of $\mathcal{P}_{\text{pre}}(\mathbf{r}|\mathbf{r}')d^3r'$.

4.3.2. Diagnostic Equations for Regenerated Phosphate

[36] Once we have computed P_{pre}, it is straightforward to use equation (15) to determine P_{reg}. However, we wish to also partition the regenerated phosphate according to its source region in the euphotic layer. To obtain the equation for P_{reg}, we recognize that in equilibrium the flux divergence of P_{reg} must be balanced by the phosphate source $\kappa\mathcal{P}_O(\mathbf{r}|\mathbf{r}')$ defined in equation (8). To zero P_{reg} on contact with the euphotic zone, where it is relabeled as preformed phosphate, an instantaneous restoring term is used in the euphotic layer. The resulting equation for P_{reg} in continuous form is the partial differential equation

$$[\mathcal{T} + \gamma_a]\mathcal{P}_{\text{reg}}(\mathbf{r}|\mathbf{r}') = \kappa\mathcal{P}_O(\mathbf{r}|\mathbf{r}'), \tag{17}$$

subject to no-flux boundary conditions on all domain boundaries including the sea surface.

[37] The discretized matrix equation corresponding to (17) is

$$[\mathbf{T} + \gamma_a]\mathbf{P}_{\text{reg}} = \kappa\mathbf{P}_O. \tag{18}$$

[38] Only columns of $\mathbf{P}_{\text{pre}}$ and $\mathbf{P}_{\text{reg}}$ corresponding to the n_s source ($\mathbf{r}'$) grid boxes in the euphotic layer are not identically zero. The preformed or regenerated phosphate originating from a particular surface region is then obtained by summing the columns corresponding to grid boxes in the region. The total preformed and regenerated phosphate fields are thus recovered by integrating over all $\mathbf{r}'$, that is, by summing over all the columns of $\mathbf{P}_{\text{pre}}$ and $\mathbf{P}_{\text{reg}}$, i.e., $P_{\text{pre}} = \mathbf{P}_{\text{pre}}\mathbf{1}$ and $P_{\text{reg}} = \mathbf{P}_{\text{reg}}\mathbf{1}$.

4.3.2.1. Results

[39] Solving (15) and (18), we find that 39% of the oceanic phosphate pool is regenerated and 61% is preformed. A similar decomposition based on the AOU data of the 2009 WOA, assuming $R_{O_2:P} = 170$, yields a slightly higher regenerated pool with 41% regenerated and 59% preformed. This difference is consistent with the analysis of *Ito et al.* [2004], which

showed that because of significant oxygen disequilibrium with the atmosphere in surface waters AOU tends to systematically overestimate respiration, but the agreement is most likely fortuitous, given the uncertainties associated with each decomposition method. Our estimates of the total amounts of preformed and regenerated phosphate are listed in Table 1, along with their uncertainties obtained by propagating assigned uncertainties in the three biogeochemical model parameters, b, σ, and κ. [A similar transport decomposition based on a data-assimilated model without any DOP, in other words with $\sigma = 0$ and $\kappa \to \infty$, and with a nutrient restoring parameterization for biological production resulted in 50% of the phosphate being regenerated pool [*DeVries et al*., 2012].

[40] The distribution of preformed nutrients (Figure 4, middle column) is closely related to the distribution of the world ocean's major water masses [e.g., compare the distribution of preformed phosphate to the distribution of Antarctic water in Figures 8 and 9 in *DeVries and Primeau*, 2011]. The bulk of the preformed nutrients come from the SO, where elevated surface phosphate concentrations (see Figure 5) are transported into the ocean interior by the formation of deep and intermediate waters. By contrast, the North Atlantic deep-water formation region supplies relatively little preformed nutrients to the interior. Except for the subtropical thermocline waters, which have relatively low preformed phosphate concentrations, and the upper water column of the North Pacific which has relatively high preformed phosphate concentrations, the bulk of the Indian and Pacific basins away from the SO have preformed phosphate concentrations that are intermediate between the low concentrations associated with North-Atlantic deep waters and the high concentrations associated with intermediate and deep waters formed in the SO.

[41] Regenerated nutrient concentrations are generally low in the Atlantic and SO and highest in the thermocline of the northern parts of the Pacific and Indian basins (Figure 4, right column). The large-scale distribution of regenerated nutrients bears some resemblance to the large-scale water-age distribution. (For convenience, Figure 6 shows the ideal water-age distribution computed from our model using the methodology described in *DeVries and Primeau* [2011]). Because particle transport and subsequent remineralization continually inject phosphate into interior water parcels, fluid elements tend to accumulate regenerated phosphate as they age. There are, however, important differences between the ideal mean age and regenerated phosphate patterns because of the spatial variations in the remineralization rate—only in the case of spatially uniform remineralization would one expect P_{reg} to be proportional to the age. The regenerated phosphate field is loaded more strongly in the thermocline than the ideal mean age pattern, consistent with the fact that most of the organic matter remineralizes in the upper water column (see Figure 3). Also, in the tropics where export production is strongest, both the Pacific and Atlantic zonal averages of P_{reg} have a local maximum in the tropics that is absent in the ideal mean-age pattern.

5. SO Uptake Perturbations: Equilibrium Response and Nutrient Trapping

[42] The SO is an important water-mass formation region [e.g., *DeVries and Primeau*, 2011]. For our data-assimilated model, approximately 56% of the ocean's water masses were last in contact with the surface south of 40°S. The SO also has some of the highest surface phosphate concentration in the world (see Figure 5), and we estimate that ~75% of the preformed phosphate inventory originates from waters ventilated south of 40°S. To examine how increasing the utilization of these nutrients would change the efficiency of the biological pump and how it would affect the flow of nutrients that feeds biological production in parts of the ocean remote from the SO (see *Holzer and Primeau* [2012] for a detailed analysis of the associated paths and timescales), we prescribed idealized perturbations by scaling up the production rate constant field γ in the SO euphotic zone. Similar perturbation experiments have been reported by *Sarmiento et al*. [2004] and *Marinov et al*. [2006]. Here we explore production perturbations with a data-constrained circulation model that should capture the transport pathways and timescales of the real ocean with greater fidelity than previous work. For example, the model circulation, used by *Sarmiento et al*. [2004] and *Marinov et al*. [2006] greatly underpredicts the uptake of CFC-11 within the SO [*Dutay et al*., 2002; *Gnanadesikan*

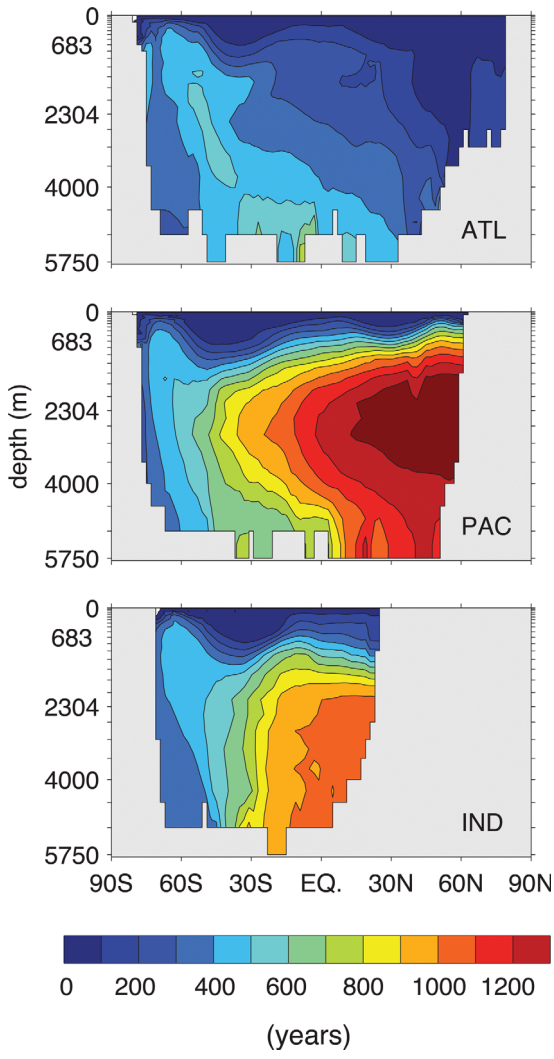

Figure 6. Zonally averaged mean age of water in the Indian, Pacific, and Atlantic basins.

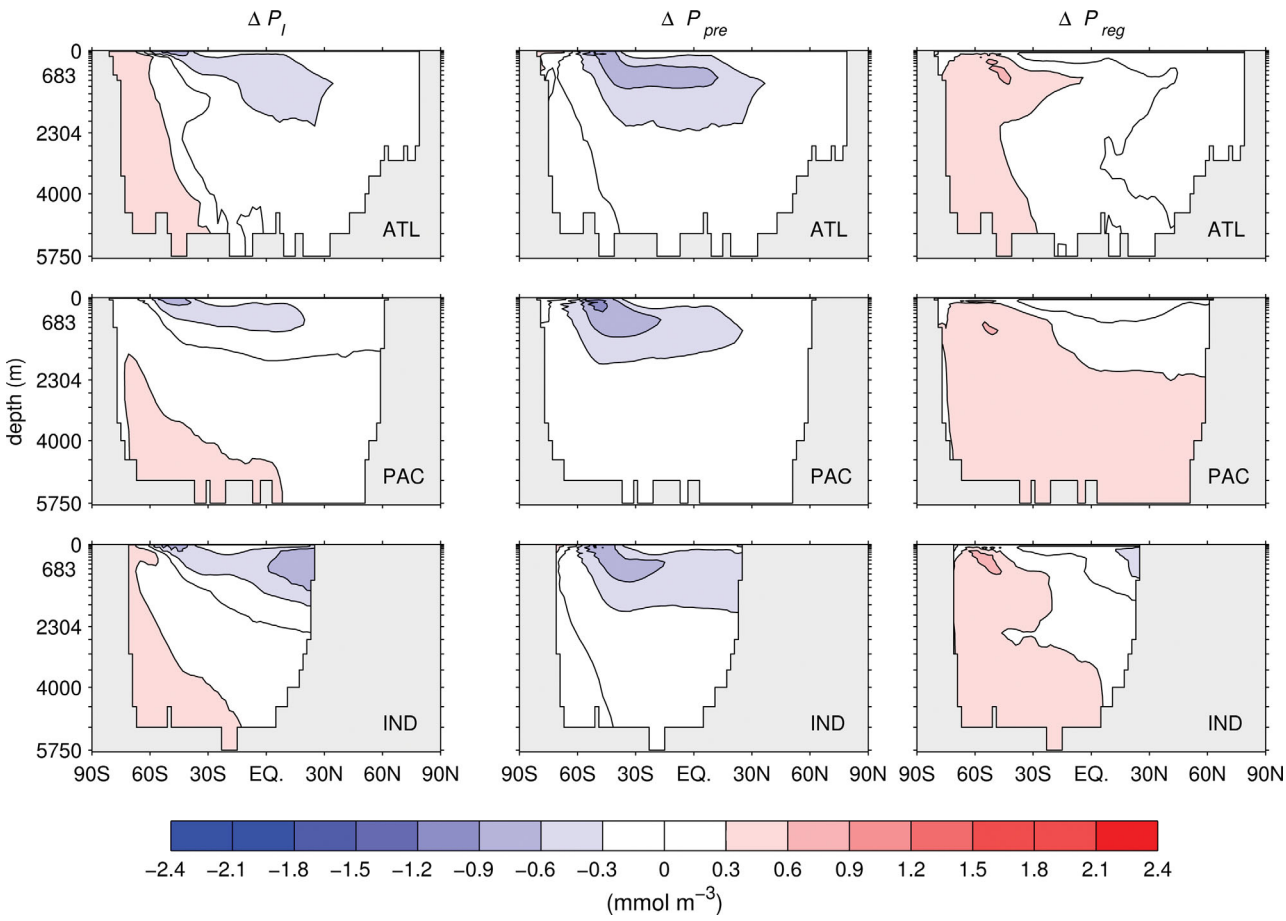

Figure 7. Change in the total (first column), preformed (second column), and regenerated (third column) phosphate concentrations due to a tenfold increase in the value of γ in the SANTZ region of the Southern Ocean. All the graphs show basinwise zonal averages of the anomalies.

et al., 2002], whereas our model circulation, being constrained by the CFC-11 observations, does very well at representing the invasion of CFCs into the ocean.

[43] Because the transport pathways and timescales of exported phosphate depend on whether the export feeds into the Antarctic deepwater formation region or into the sub-Antarctic intermediate and mode-water formation region [*Marinov et al*., 2006], we divided the surface south of 40°S into an Antarctic zone (ANTZ) and a sub-Antarctic zone (SANTZ). The northern boundary of the SANTZ is arbitrary, but lies close to the northernmost edge of the high-surface nutrient region of the SO. We defined the boundary between the ANTZ and the SANTZ to be the latitude of maximum Ekman divergence, computed using the NCEP wind-stress climatology [*Trenberth et al*., 1989] that was used in the assimilation. The ANTZ and SANTZ regions are shown in Figure 5 superimposed on the contour plot of the averaged phosphate concentration in the top 73.4 m.

[44] The ANTZ has low export production in spite of its high PO_4 concentration accounting for less than 3.5% of the globally integrated export production and less than 3% of the ocean's regenerated phosphate inventory. Correspondingly, waters ventilated from the ANTZ contribute more than 43% of the ocean's preformed phosphate inventory. The SANTZ is a region of strong surface phosphate gradient. Phosphate decreases northward as biological production strips out phosphate from Ekman-driven northward flow. Waters ventilated from the SANTZ contribute ~31% of the preformed phosphate inventory. Biological production in the SANTZ is relatively high, accounting for ~23% of the globally integrated export production and ~17% of the regenerated phosphate inventory. Table 1 summarizes the percentages and their uncertainties.

[45] We focus on two particular perturbations: one in which we scaled up γ by a factor of 10 in the SANTZ, leaving it unchanged in the rest of the ocean, and one in which we scaled up γ by a factor of 100 over the ANTZ, again leaving it unchanged in other parts of the ocean. Both cases produced comparable SO-averaged γ values: $\overline{\gamma}_{SO} = (135\text{ days})^{-1}$ for the $10 \times \gamma(\text{SANTZ})$ perturbation and $\overline{\gamma}_{SO} = (147\text{ days})^{-1}$ for the $100 \times \gamma(\text{ANTZ})$ perturbation. The unperturbed optimized model had a SO-averaged uptake rate with a timescale $\overline{\gamma}_{SO} = (3.5\text{ years})^{-1}$.

[46] Figure 7 shows the changes in the basin zonal average of the total, preformed, and regenerated phosphate concentrations for the perturbation experiment with the tenfold increase in γ over the SANTZ. The increase of SANTZ phosphate uptake results in an increase in the phosphate concentration in the water masses ventilated in the ANTZ accompanied by a decrease in the PO_4 of water masses

ventilated from the SANTZ and to a lesser extent those ventilated from regions north of 40°N. The decrease in phosphate concentration is most pronounced in the surface waters of SANTZ but large decreases in concentration also extend northward in the mode and intermediate waters formed in the SANTZ as well as in the upper water column in the northern part of the Indian Ocean. In the Indian and Pacific basins, the drop in concentration is confined to the upper part of the water column, whereas in the North Atlantic, the drop in concentration extends to the bottom of the ocean.

[47] Apart from the large-scale transfer of phosphate into the ANTZ-ventilated water masses, the increased nutrient utilization in the SANTZ produces a transfer of phosphate from the preformed pool into the regenerated pool for most of the ocean. Exceptions are the North Atlantic, the upper part of the northern Indian Ocean, and the surface waters to the north of 40°S, all of which experience decreases in both P_{pre} and P_{reg}. In water masses ventilated from the SANTZ (sub-Antarctic-mode water and Antarctic-intermediate waters), there is a strong decrease in preformed phosphate accompanied by a partly compensating increase in regenerated phosphate. The compensation is only partial because part of the increase in organic matter production in the euphotic zone of the SANTZ is exported into deeper water masses that are ventilated from outside the SANTZ.

[48] The export production in the SANTZ injects organic matter into the southward flowing waters at middepth, which short-circuits northward Ekman transport of phosphate out of the SO. For example, nutrients regenerated in North Atlantic deep water enter the SO at depth where they are either entrained into Antarctic bottom water, perhaps after upwelling to the ANTZ surface or are upwelled into the SANTZ, where they are again stripped out by biological production. This results in a gradual accumulation of phosphate into circumpolar and deep waters that must eventually be balanced by eddy diffusive fluxes out of ANTZ-ventilated waters (Figure 8). We call this SO nutrient trapping.

[49] The SO nutrient trapping also manifests itself for the $100 \times \gamma(\mathrm{ANTZ})$ perturbations. Increased nutrient drawdown in the ANTZ decreases the amount of nutrients that can be diffused by eddies into the SANTZ and transported out of the SO by northward flowing Ekman currents. Figure 9 shows the changes in the zonal-averaged total, preformed, and regenerated phosphate concentrations. The pattern for the change in the total phosphate concentration is similar to that of the $10 \times \gamma(\mathrm{SANTZ})$ perturbation experiment, but the transfer between preformed and regenerated pools is quite different. The $100 \times \gamma(\mathrm{ANTZ})$ perturbation transfers a much larger amount of phosphate from the preformed to the regenerated pool. For the $100 \times \gamma(\mathrm{ANTZ})$ perturbation, all water masses show a decrease in preformed phosphate, whereas for the $10 \times \gamma(\mathrm{SANTZ})$ perturbation, there was a modest increase in the preformed phosphate for ANTZ-ventilated water masses. The compensating increase in regenerated nutrients observed for the $100 \times \gamma(\mathrm{ANTZ})$ perturbation experiments is strongest in the deep waters of the SO but extends northward in all the basins becoming progressively weaker, until, in the upper thermocline, there is actually a decrease in regenerated phosphate that reinforces the decrease in preformed phosphate.

[50] The drop in phosphate in the surface waters north of 40°S, observed for both the $100 \times \gamma(\mathrm{ANTZ})$ and the $10 \times \gamma(\mathrm{SANTZ})$ perturbation experiments, results in 20%–30% decreased biological production north of 40°S (Figure 10). While the perturbed equilibrium production maintains its original pattern, the percentage decrease shown in Figure 10 has remarkably little structure in each basin, although the response is weakest in the Pacific, strongest in the Atlantic, and intermediate in the Indian Ocean. The contrast between the Pacific and Atlantic is expected from the more vigorous overturning circulation of the Atlantic and the lack of significant deep-water formation in the North Pacific, which has its own large-scale high-latitude surface phosphate supply (Figure 5).

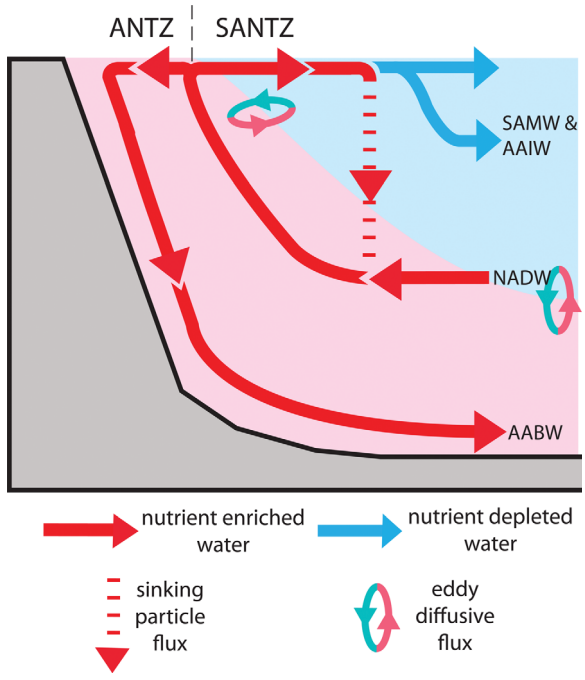

Figure 8. Schematic showing the trapping of nutrients in the SO when nutrient utilization is increased in the SO surface waters. The combination of large-scale advective transport and sinking-particle transport leads to a net convergence of nutrients in the SO waters and in waters ventilated from the ANTZ, which must eventually be balanced by the globally integrated effects of eddy-driven diapycnal mixing.

5.1. SO Nutrient Trapping and Biological Pump Efficiency

[51] The transfer from the preformed to the regenerated pool in response to increased SO nutrient uptake impacts the efficiency of the biological pump. Following *Sigman and Boyle* [2000], we define the efficiency of the biological pump as the ratio of the average regenerated phosphate concentration to the average total phosphate concentration. *Ito and Follows* [2005] demonstrated that there is a close connection between atmospheric carbon dioxide concentration and the efficiency of the biological pump defined in this way.

[52] In order to explore the sensitivity of the biological pump efficiency to changes in the SO biological production, we performed a sequence of numerical experiments in which we gradually rescaled the SO uptake rate coefficient in the ANTZ, SANTZ, and ANTZ $\cup$ SANTZ. For each

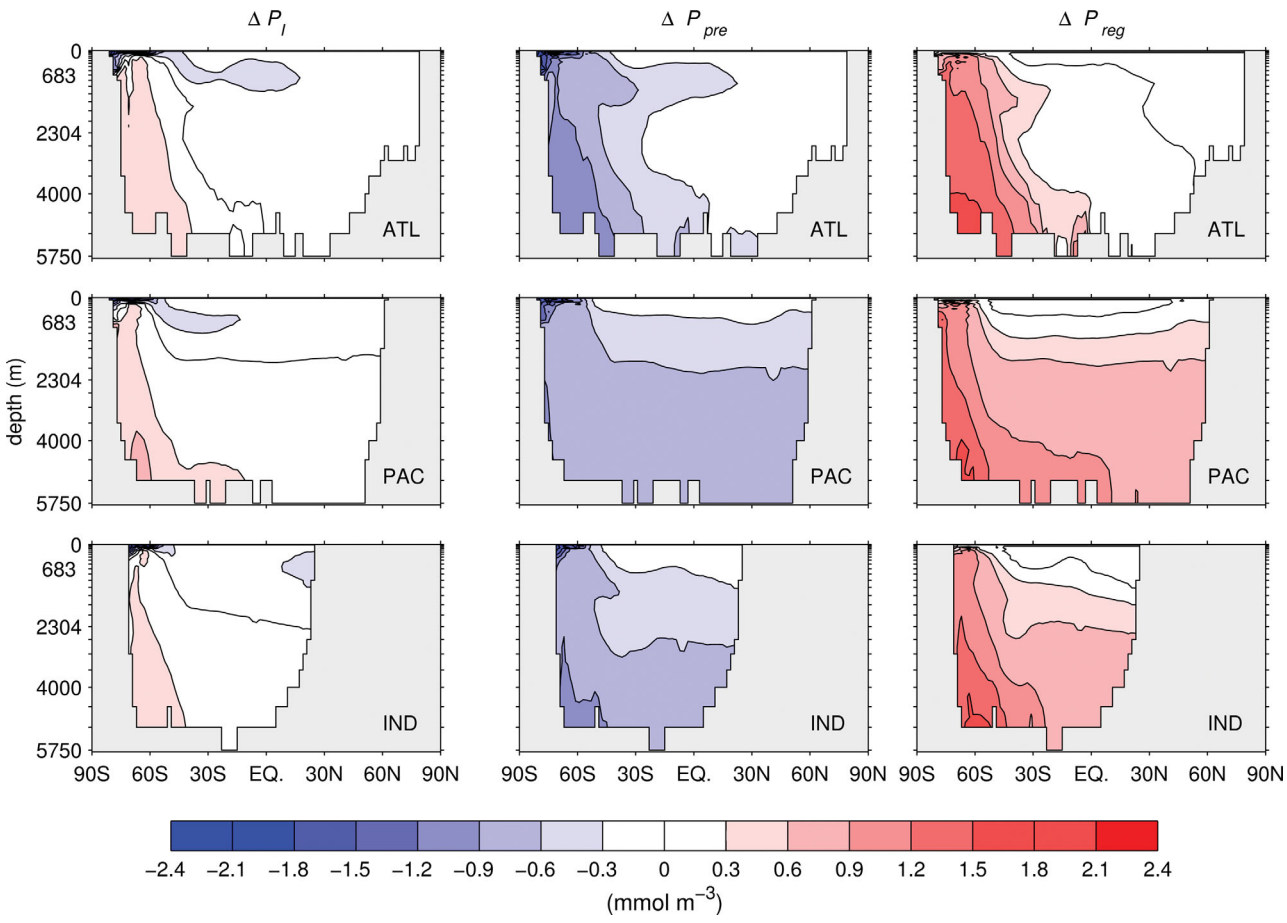

Figure 9. Change in the total (first column), preformed (second column), and regenerated (third column) phosphate concentrations due to a 100-fold increase in the value of γ in the ANTZ region of the SO. All the graphs show basinwise zonal averages of the anomalies.

perturbation region, a sequence of ∼50 equilibrium model solutions were determined to trace out the curves shown in Figures 11 and 12.

[53] Figure 11 shows the biological pump efficiency plotted as a function of the SO-averaged phosphate uptake rate, $\overline{\gamma}_{SO}$. The unperturbed state, which uses our optimized phosphate uptake rate and is therefore the most relevant to the real ocean, is indicated by the black dot: It has $\overline{\gamma}_{SO} = (3.5 \text{ years})^{-1}$, and a biological pump efficiency of only 39%. Scaling the $\overline{\gamma}_{SO}$ down to zero decreases the biological pump efficiency by only ∼4% to 35%, whereas scaling $\overline{\gamma}_{SO}$ up until the average nutrient uptake timescale is less than 1 day increases the efficiency to ∼95% (Figure 11, solid curve).

[54] For the ANTZ-only perturbation, the biological pump efficiency ranges from a minimum of ∼38% (no ANTZ production) to the asymptotic efficiency of ∼75% in the limit of infinitely fast ANTZ nutrient uptake (Figure 11, dotted curve). Interestingly, the maximum efficiency for the ANTZ perturbation of 77% occurs for a finite SO-average uptake timescale of ∼11 days. (A detailed investigation of this effect is beyond the scope of this paper).

[55] Scaling up γ in the SANTZ leads to a maximum efficiency of 58% for an uptake timescale of ∼11 days before reaching the asymptotic 57% efficiency in the limit where $\overline{\gamma}_{SO} \to \infty$ (Figure 11 dashed curve). Decreasing the uptake rate over the SANTZ leads to a modest reduction in the efficiency of the biological pump, which asymptotes to a ∼35% efficiency in the limit where $\gamma(\text{SANTZ}) \to 0$. Scaling down the value of γ over the combined ANTZ ∪ SANTZ regions produces essentially the same result as scaling down the value of γ over the SANTZ region alone, consistent with the fact that the reference equilibrium has very low ANTZ biological productivity.

[56] Figure 11 also shows that decreasing the SANTZ timescale increases the biological pump efficiency less than decreasing the ANTZ timescale for a given decrease in γ^{-1}. This is in spite of the fact that SANTZ is more than 3 times larger than ANTZ. This confirms the findings of *Marinov et al*. [2006] that ANTZ perturbations are much more effective than SANTZ perturbations for changing biological pump efficiency.

[57] Finally, from Figure 11 we can see that there is a considerable amount of interaction between the ANTZ perturbation and the SANTZ perturbation. The response of the ANTZ ∪ SANTZ perturbation (solid curve) is not the sum of the ANTZ-only (dotted curve) and SANTZ-only (dashed curve) responses. As nutrients are drawn down in one region, the transport of preformed and regenerated nutrients are altered, which affects production in neighboring regions and, as we show in the next section, in the rest of the ocean.

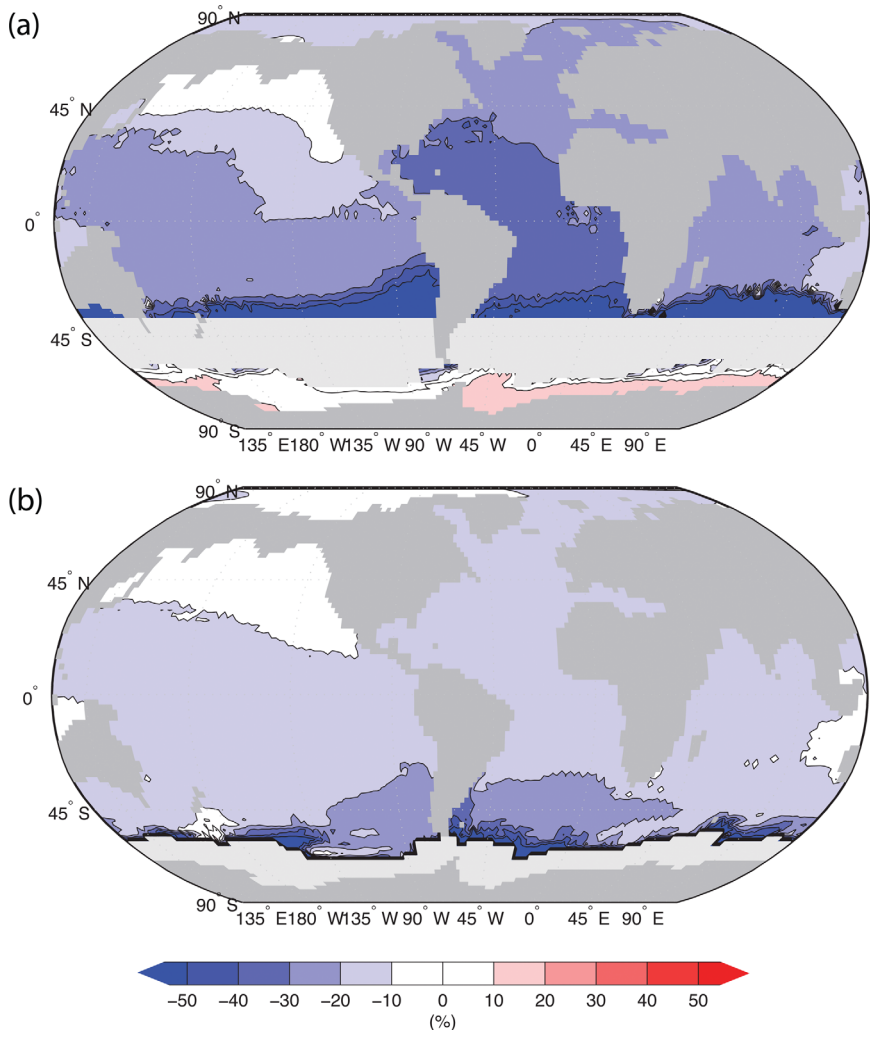

Figure 10. Relative change in export production in remote regions due to (a) a 10 times increase in the value of γ in the SANTZ and (b) a 100 times increase in the value of γ in the ANTZ. The region where the scaling perturbation was applied is shaded in light gray.

5.2. SO Nutrient Trapping and Global Production

[58] The large-scale redistribution of nutrients that results from changes in SO nutrient uptake also affects biological production over the rest of the ocean. Figure 12 shows the production (J) and the new production (J_{new}) integrated over the SO (ANTZ $\cup$ SANTZ) and over the complementary region to the north of 40°S as a function of the SO-averaged phosphate uptake rate, $\overline{\gamma}_{SO}$. The export production (J_{ex}), not shown explicitly, is indistinguishable from the new production when integrated over the same regions, the maximum relative difference being ~1%. The unperturbed state is indicated by the red and blue dots at $\overline{\gamma}_{SO} = (3.5 \text{ years})^{-1}$: in the region south of 40°S unperturbed production is 2.5 Pg C/yr and unperturbed new production is 1.9 Pg C/yr. In the region north of 40°S unperturbed production and new production are 8.1 Pg C/yr and 5.4 Pg C/yr, respectively (assuming a C:P ratio 106). Scaling the $\overline{\gamma}_{SO}$ down to zero to shut off biological production south of 40°S increases biological production in the region north of 40°S by 12% to 9.1 Pg C/yr, while new production is increased by 13% to 6.2 Pg C/yr. Scaling $\overline{\gamma}_{SO}$ up until the average nutrient uptake timescale is less than 1 day decreases all measures of production (J, J_{new}, and J_{ex}) north of 40°S by ~44%. To the south of 40°S, production increases by ~727%, while the new and export productions increase by ~644%. The large increase in production in the SO accompanied by a decrease in the region to the north of 40°S is a manifestation of SO nutrient trapping, which we explore further in a separate publication [*Holzer and Primeau*, 2012]. Interestingly, in all our experiments, we found that the globally integrated production increased as we increased the efficiency of SO nutrient utilization. This is in contrast to the GCM study of *Marinov et al.* [2006], which found that in some cases increasing the SO nutrient utilization rate moved the global phosphate distribution to greater depths, which led to a decrease in the globally integrated production.

[59] The concept of a biogeochemical divide [*Marinov et al.*, 2006] is also evident in the global production fields associated with our perturbation experiments: in the limit of infinitely fast nutrient uptake, SANTZ-only perturbations decrease production in the region north of 40°S by

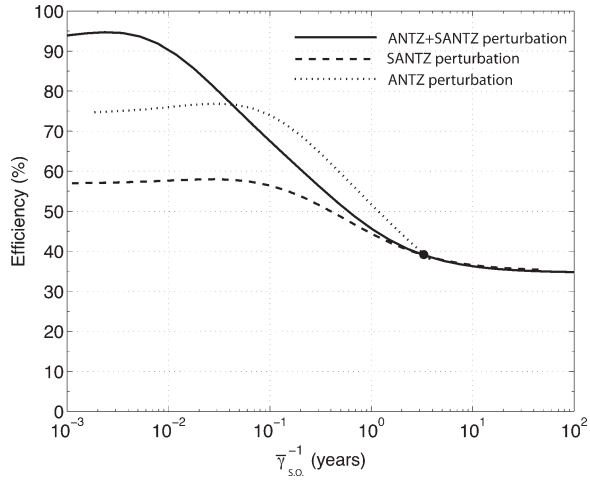

Figure 11. Efficiency of the biological pump as a function of the phosphate uptake rate averaged over the union of the ANTZ and SANTZ, $\overline{\gamma}_{SO}$, expressed as an uptake timescale. The black circle indicates the reference simulation that is most relevant to the real ocean. The dotted curve indicates the case where the production rate coefficient, γ, is scaled up or down in the ANTZ region. The dashed curve indicates the case where γ is scaled up or down in the SANTZ region, and the solid curve corresponds to the case where γ is scaled up or down in the combined ANTZ and SANTZ.

41% while ANTZ-only perturbations decrease production by only 14%, confirming that the region to the north of the maximum Ekman divergence have a larger effect on biological production outside the SO. The corresponding SO production increase due to the SANTZ-only and ANTZ-only perturbations is 487% and 358% in the limit of infinitely fast uptake.

6. Discussion

[60] In qualitative agreement with the early ocean GCM simulations of *Sarmiento and Orr* [1991], increasing the biological phosphate uptake rate in the SO causes a large-scale transfer of phosphate from the preformed to the regenerated pool and a large-scale transfer of phosphate to circumpolar and deep waters. In our model, complete SO nutrient utilization increases the biological pump efficiency to 94%. Completely shutting down biological production in the SO decreases the pump efficiency from 39% to 36%. This small reduction suggests that the SO waters contribute very little to the overall efficiency of the contemporary ocean's biological pump, consistent with the whole-ocean nutrient drawdown numerical experiments of *DeVries et al.* [2012]. The large increase in efficiency with complete SO nutrient utilization supports, in the context of a data-constrained circulation model, the potentially important role played by the high-latitude ocean in controlling the large glacial-interglacial swings in atmospheric carbon dioxide [e.g., *Knox and McElroy*, 1984; *Sarmiento and Toggweiler*, 1984; *Siegenthaler and Wenk*, 1984]. Atmospheric CO_2 varies by 300 ppmv between minimum and maximum biological pump efficiency [*Ito and Follows*, 2005], suggesting that the biological pump must have operated at 72% efficiency during glacial times to account for the lower glacial atmospheric CO_2. (Atmospheric pCO_2 was approximately 180 ppm during glacial periods and 280 ppm during interglacial periods [*Petit et al.*, 1999]). Our results suggest that without any changes in the circulation, a complete drawdown of nutrients in the SANTZ alone is insufficient to

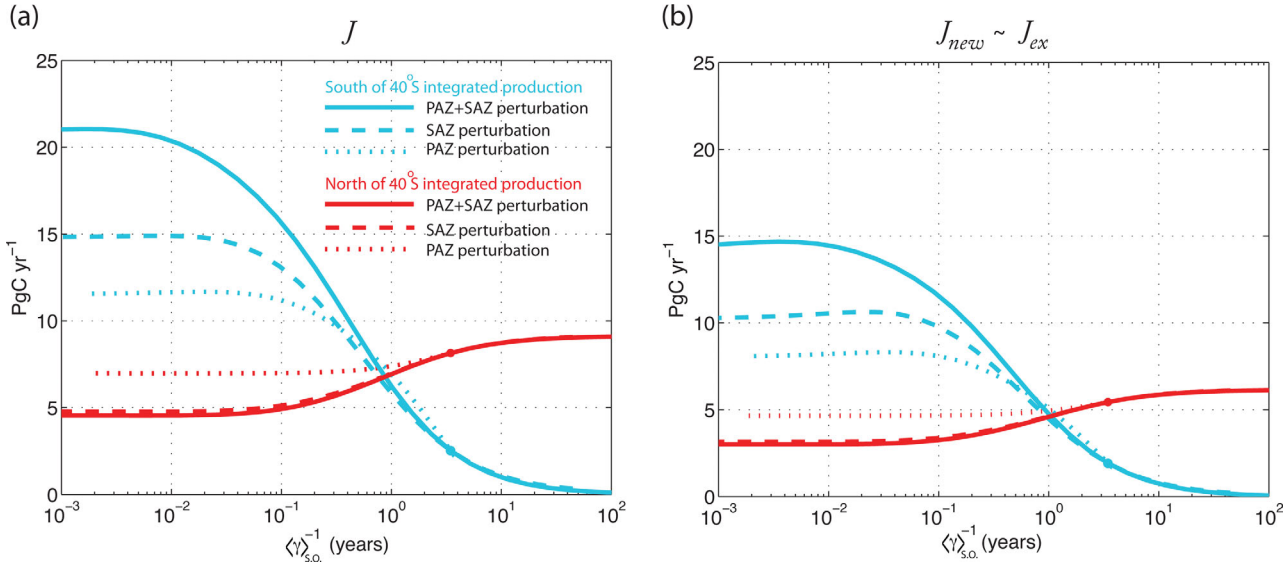

Figure 12. (a) Biological production integrated over the region south of 40°S (blue curves) and over the region north of 40°S (red curves). (b) New production integrated over the same regions. The solid curves correspond to the experiments in which γ was perturbed in the combined SANTZ $\cup$ ANTZ region. The dashed curves correspond to experiments in which γ was perturbed in only the SANTZ, and the dotted curves correspond to the case where γ was perturbed in ANTZ. A C:P ratio of 106 was used to convert the phosphate uptake rate into the more familiar carbon production units.

account for the full glacial-interglacial atmospheric CO_2 variations, but that complete drawdown in the ANTZ alone or over the whole SO would be sufficient.

[61] The large increase in efficiency with increased nutrient uptake in the SO is a consequence of SO nutrient trapping: Increased biological production causes strongly enhanced short circuiting of the Ekman-driven northward transport of nutrients through the export of organic phosphorus by sinking particles, which remineralize at mid-depth in southward flowing water masses. As a result, nutrients get trapped in circumpolar and deep waters. This trapping sustains a dramatically increased production in the SO and starves the rest of the ocean where production decreases in response. We find that complete SO-nutrient drawdown causes production to decrease by 44% north of 40°S and to increase by more than 725% in the SO.

[62] In accord with the concept of a biogeochemical divide [*Marinov et al*., 2006] and with the regional differences in sequestration efficiency documented in *DeVries et al*. [2012], we find that production perturbations in the SANTZ are more effective at transferring nutrients to circumpolar and deep waters by producing a stronger SO nutrient trapping while production perturbations in the ANTZ are more effective at transferring nutrients from the preformed pool to the regenerated pool and, therefore, more effective at increasing the efficiency of the biological pump.

7. Summary and Conclusions

[63] We have constructed a linear data-assimilated model for the ocean's phosphorus cycle to quantify SO nutrient trapping, the efficiency of the biological pump, and how these respond to perturbations in SO productivity. The data assimilation jointly optimized the model's physical transport, biological production, and exponent in the power law parameterization for sinking particulate organic matter, to obtain an improved view of the cycling of phosphorus in the ocean.

[64] We estimate that the efficiency of the biological pump is (39±7)% in the present-day ocean, with much of the biological pump's leak originating in the SO, where (75±4)% of the preformed phosphate inventory and only (20±4)% of the regenerated phosphate inventory originate. However, the disproportionate amount of preformed nutrients originating from the SO does not imply low export production in that part of the ocean. We find that the region south of 40°S accounts for (26±6)% of the estimated 7.4±2.5 Pg C/yr global export production. Our estimate is consistent with that of *Schlitzer* [2002], who estimated that the region south of 30°S exports 2 Pg C/yr. (We estimate 1.8±0.4 Pg C/yr for the same region).

[65] In this study, we focused on quantifying the data-assimilated model's equilibrium phosphorus cycle, biological sources and sinks of phosphate, and global-scale responses to SO productivity perturbations. The patterns, pathways, and timescales with which SO productivity is connected to the biological production in the rest of the world ocean is explored in the context of our data-assimilated model by *Holzer and Primeau* [2012]. In both studies, we exploit the computational efficiencies afforded by the linearity of our steady-state model and its matrix formulation, a key advantage of our approach.

[66] The use of a data-assimilated model allowed us to make inferences about the cycling of phosphorus in the real ocean. Our model eliminates some of the SO ventilation biases that were apparent in simulated CFC-11 in previous models [e.g., *Sarmiento et al*., 2004; *Marinov et al*., 2006]. Nevertheless, it is important to keep in mind the limitations of our analysis. Our uncertainty analysis was limited to propagating prescribed uncertainties in the three phosphorus-cycling parameters, σ, κ, and b, and while we did take into account data uncertainties in the optimization of the transport operator, we did not propagate the uncertainties of the resulting operator into uncertainties for our biogeochemical inferences. In principle, the transport operator uncertainties could have been taken into account using a Monte Carlo analysis similar to the one used in *DeVries and Primeau* [2011], but the higher resolution of our model and the larger number of tracers, including the transient CFC-11 and the coupled PO_4 and DOP tracers, made this computationally too expensive. We tried to compensate for this by assigning large uncertainty ranges to the biogeochemical parameters but substantial uncertainty remains in our transport estimates because of the coarse resolution of our model and because of the lack of an explicitly resolved seasonal cycle. We expect that our model captures the export into the permanent thermocline better than the export into the seasonal thermocline, where both transport and biological production have strong seasonal variations. Furthermore, by keying production to a single limiting nutrient, namely phosphate, we ignored the potentially rich and complex ecosystem dynamics that can occur in more complex biogeochemical models with multiple limiting nutrients and multiple functional groups [e.g., *Moore et al*., 2004; *Le Quéré et al*., 2005]. In the future, we plan to add nitrogen, silicate, dissolved inorganic carbon, and oxygen to our data-assimilated model to obtain even better biogeochemical constraints and at the same time explore how multiple limiting nutrients might modify how production perturbations in one part of the ocean can impact production in other parts of the ocean.

Appendix A: Parameter Sensitivity

[67] Our simple phosphorus cycling model has three biogeochemical parameters: σ, κ, and b. To study the sensitivity of the optimized phosphorus cycle solution to perturbations in these parameters, we compute the derivative of the equilibrium model solution with respect to the parameters using a finite difference approach. Figure A1 shows the relative sensitivity of the equilibrium preformed and regenerated phosphate concentrations to a relative change in the value of the exponent b in the Martin power law. Figure A2 shows the relative sensitivity of the equilibrium preformed and regenerated phosphate concentrations to a relative change in the proportion, σ, of production allocated directly to the DOP pool in the euphotic layer. Figure A3 shows the relative sensitivity of the equilibrium preformed and regenerated phosphate concentrations to a relative change in the remineralization rate, κ, of organic phosphorus. By far, the largest sensitivities are due to the power-law exponent b.

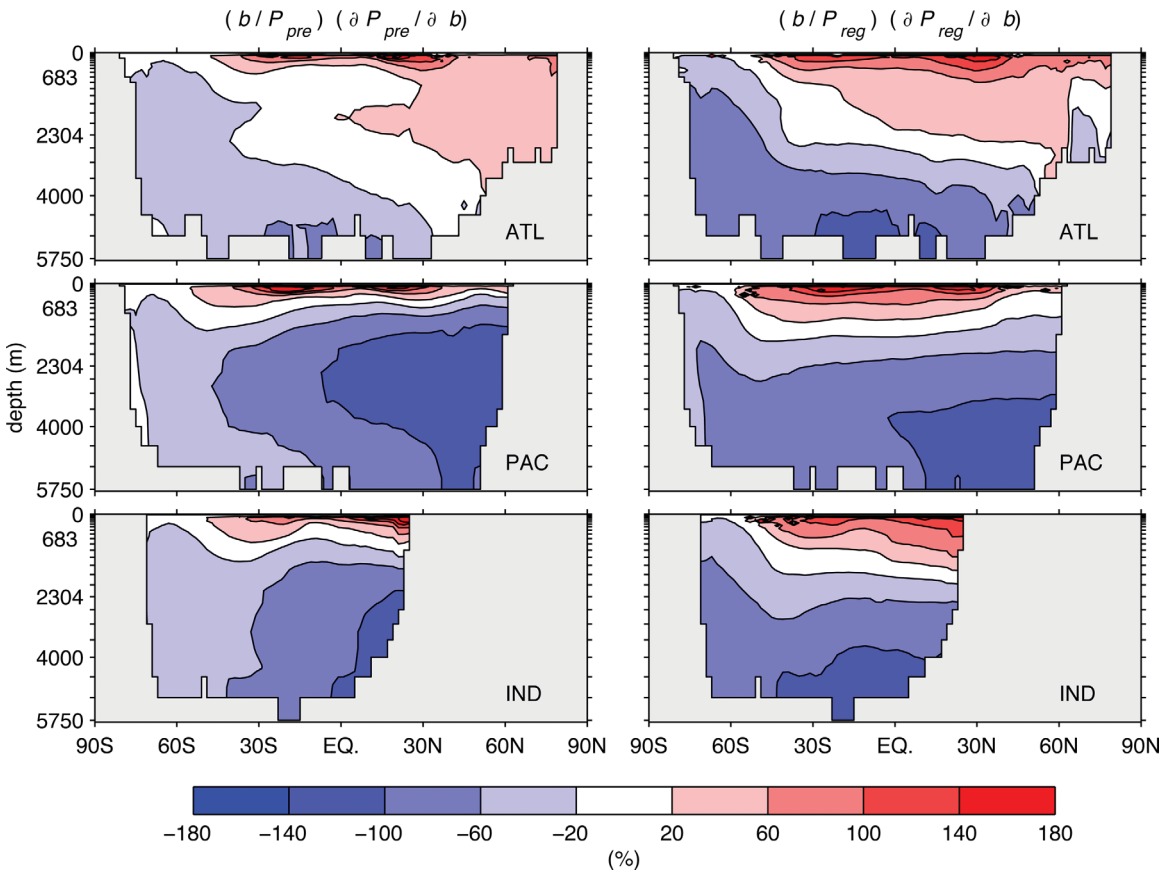

Figure A1. Relative sensitivity of the equilibrium preformed and regenerated phosphate concentrations to a relative change in b. Zonal averages for the Atlantic, Pacific, and Indian basins are shown.

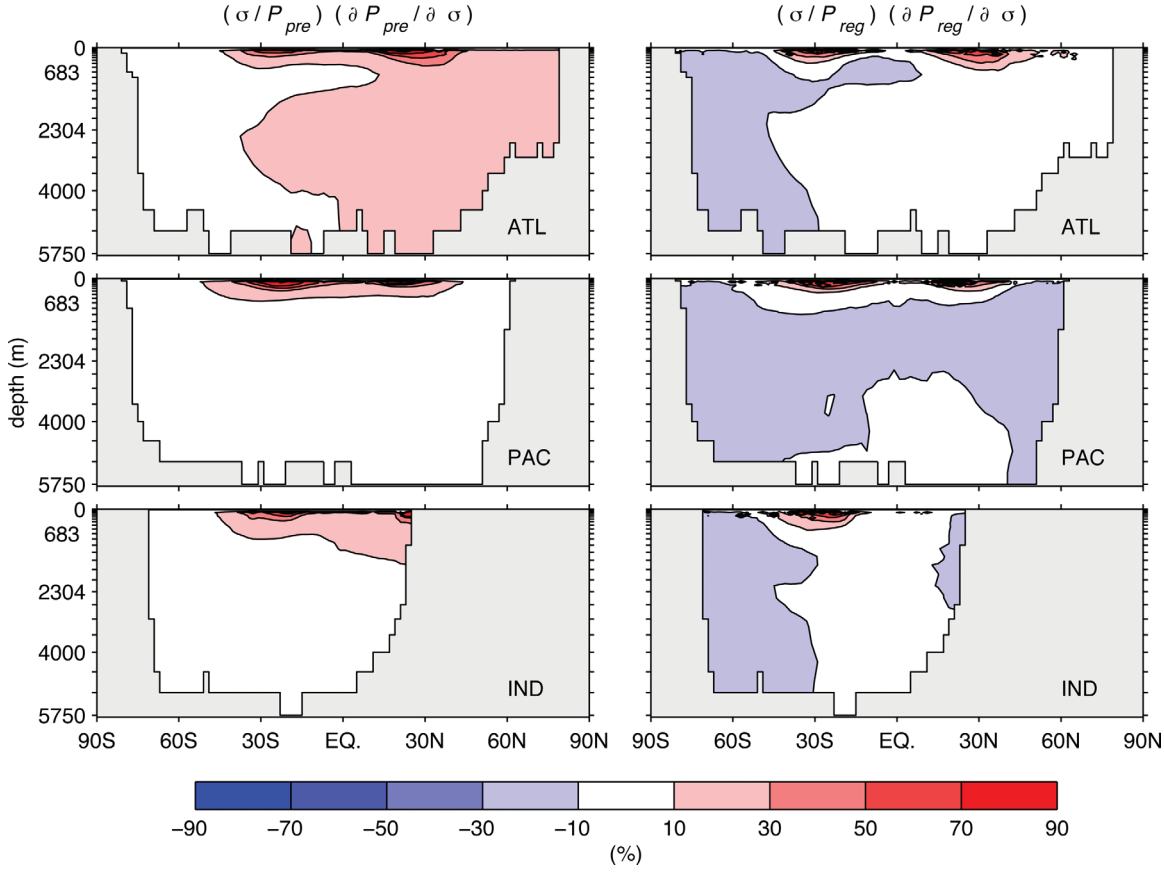

Figure A2. Relative sensitivity of the equilibrium preformed and regenerated phosphate concentrations to a relative change in σ. Zonal averages for the Atlantic, Pacific, and Indian basins are shown.

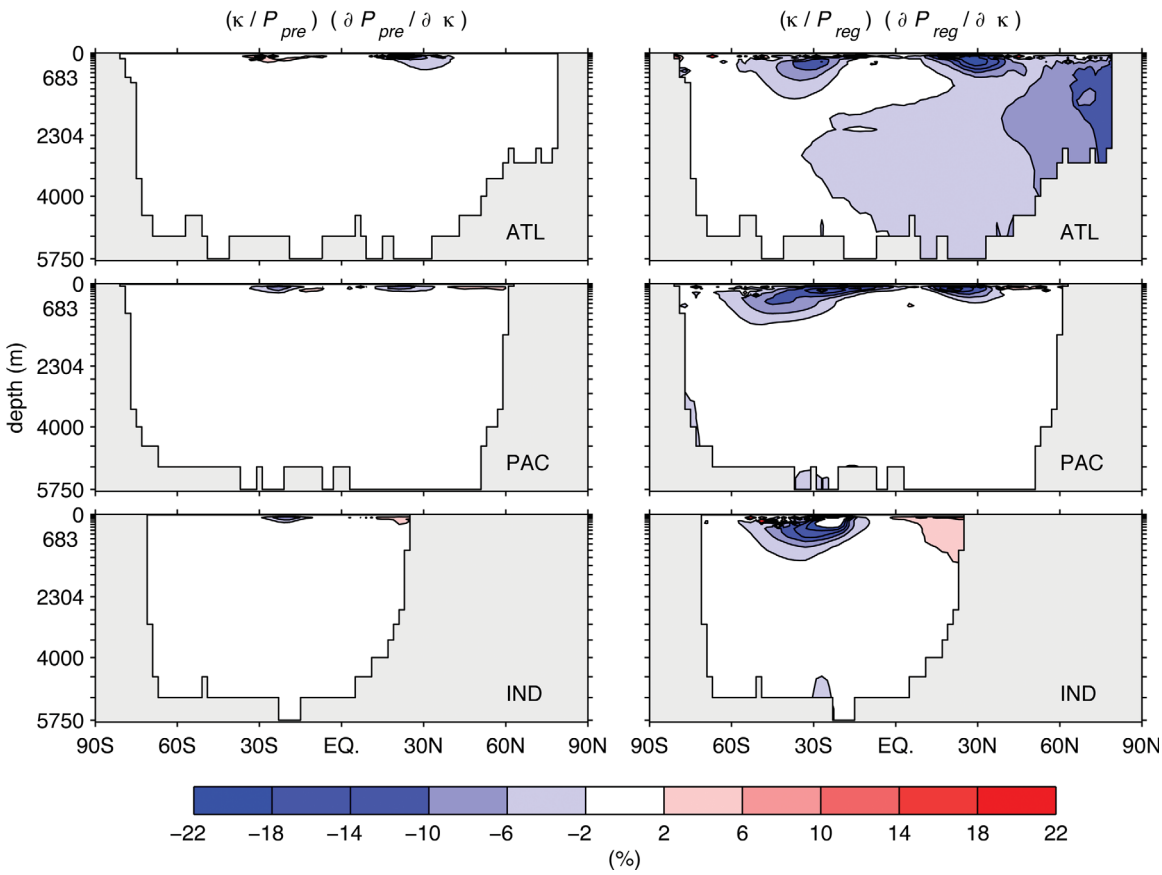

Figure A3. Relative sensitivity of the equilibrium preformed and regenerated phosphate concentrations to a relative change in κ. Zonal averages for the Atlantic, Pacific, and Indian basins are shown.

[68] **Acknowledgments.** This work was supported by NSF grant OCE-1131768 (FP), by ARC grant DP120100674, and NSF grant ATM-0854711 (M.H). T.D. acknowledges support from grant OCE-1131548 awarded to Curtis Deutch at UCLA. M.H. also acknowledges a UNSW faculty research grant.

References

Abell, J., S. Emerson, and P. Renaud (2000), Distribution of TOP, TON, and TOC in the North Pacific subtropical gyre: Implications for nutrient supply in the surface ocean and remineralization in the upper thermocline, *J. Mar. Res.*, *58*, 203–222.

Botev, Z., J. Grotowski, and D. Kroese (2010), Kernel density estimation via diffusion, *Ann. Stat.*, *38*(5), 2916–2957.

DeVries, T., and F. Primeau (2011), Dynamically and observationally constrained estimates of water-mass distributions and ages in the global ocean, *J. Phys. Oceanogr.*, *41*(12), 2381–2401, doi:10.1175/JPO-D-10–05011.1, 2011.

DeVries, T., F. Primeau, and C. Deutsch (2012), The sequestration efficiency of the biological pump, *Geophys. Res. Lett.*, *39*, L13601, doi:10.1029/2012GL051963.

Dutay, J. C., et al. (2002), Evaluation of ocean model ventilation with CFC-11: Comparison of 13 global ocean models, *Ocean Modell.*, *4*(2), 89–120, doi:10.1016/S1463–5003(01)00013-0.

Duteil, O., et al. (2012), Preformed and regenerated phosphate in ocean general circulation models: can right total concentrations be wrong? *Biogeosciences*, *9*, 1797–1807, doi:10.5194/bg-9-1797-2012.

Dutkiewicz, S., M. Follows, and P. Parekh (2005), Interactions of the iron and phosphorus cycles: A three-dimensional model study, *Global Biogeochem. Cycles,*, *19*, doi:10.1029/2004GB002342.

Garcia, H. E., R. A. Locarnini, T. P. Boyer, and J. I. Antonov (2010a), *World Ocean Atlas 2009, vol. 3. Dissolved Oxygen, Apparent Oxygen Utilization, and Oxygen Saturation*, edited by S. Levitus, p. 344, U.S. Gov. Print. Off., Wash., D. C.

Garcia, H. E., R. A. Locarnini, T. P. Boyer, and J. I. Antonov (2010b), *World Ocean Atlas 2009, vol. 4. Nutrients (Phosphate, Nitrate, and Silicate)*, edited by S. Levitus, p. 398, U.S. Gov. Print. Off., Wash., D. C.

Gnanadesikan, A., R. Slater, N. Gruber, and J. Sarmiento (2002), Oceanic vertical exchange and new production: A comparison between models and observations, *Deep Sea Res. II*, *49*, 363–401.

Holzer, M., and F. Primeau (2012), Global teleconnections in the oceanic phosphorus cycle: Patterns, paths, and timescales, *J. Geophys. Res. Oceans*, *118*, doi:10.1002/jgrc.20072.

Ito, T., and M. J. Follows (2005), Preformed phosphate, soft tissue pump and atmospheric CO_2, *J. Mar. Res.*, *63*, 813–839.

Ito, T., M. J. Follows, and E. A. Boyle (2004), Is AOU a good measure of respiration in the oceans?, *Geophys. Res. Lett.*, *31*, L17305, doi:10.1029/2004GL020900.

Key, R. M., A. Kozyr, C. L. Sabine, K. Lee, R. Wanninkhof, J. L. Bullister, R. A. Feely, F. J. Millero, C. Mordy, and T.-H. Peng (2004), A global ocean carbon climatology: Results from Global Data Analysis Project (GLODAP), *Global Biogeochem. Cycles*, *18*, GB4031, doi:10.1029/2004GB002247.

Knox, F., and M. B. McElroy (1984), Changes in atmospheric CO_2: Influence of the marine biota at high latitude, *J. Geophys. Res.*, *89*, 4629–4637, doi:10.1029/JD089iD03p04629.

Kwon, E. Y., and F. Primeau (2006), Sensitivity and optimization study of a biogeochemistry ocean model using an implicit solver and in-situ phosphate data, *Global Biogeochem. Cycles*, *20*, GB4009, doi:10.1029/2005GB002631.

Kwon, E. Y., and F. Primeau (2008), Optimization and sensitivity of a global biogeochemistry ocean model using combined in-situ DIC, alkalinity and phosphate data, *J. Geophys. Res., Oceans*, *113*, C08011, doi:10.1029/2007/JC004520.

Le Quéré, C., et al. (2005), Ecosystem dynamics based on plankton functional types for global ocean biogeochemistry models, *Global Change Biol.*, *11*, 2016–2040, doi:10.11111/j.1365–2486.2005.01004.x.

Li, X., and F. Primeau (2008), A fast Newton-Krylov solver for seasonally varying global ocean biogeochemistry models suitable for systematic parameter optimization, *Ocean Modell.*, *23*, 13–20.

Marinov, I., A. Gnanadesikan, J. R. Toggweiler, and J. L. Sarmiento (2006), The Southern Ocean biogeochemical divide, *Nature*, *441*, 964–967, doi:10.1038/nature04883.

Martin, J. W., G. A. Knauer, D. M. Karl, and W. W. Broenkow (1987), VERTEX: Carbon cycling in the NE Pacific, *Deep-Sea Res.*, *34*, 267–285.

Moore, J. K., S. C. Doney, and K. Lindsay (2004), Upper ocean ecosystem dynamics and iron cycling in a global three-dimensional model, *Global Biogeochem. Cycles*, *18*, GB4028, doi:10.1029/2004GB002220.

Oschlies, A., W. Koeve, W. Rickels, and K. Rehdanz (2010), Side effects and accounting aspects of hypothetical large-scale Southern Ocean iron fertilization, *Biogeosciences*, *7*, 4017–4035, doi:10.5194/bg-7–4017-2010.

Petit, J., et al. (1999), Climate and atmospheric history of the past 420,000 years from the Vostok ice core, Antarctica, *Nature*, *399*, 429–436.

Primeau, F. W. (2005), Characterizing transport between the surface mixed layer and the ocean interior with a forward and adjoint global ocean transport model, *J. Phys. Oceanogr.*, *35*, 545–564, doi:10.1175/JPO2699.1.

Primeau, F. (2006), On the variability of the exponent in the powerlaw depth dependence of POC flux estimated from sediment traps, *Deep Sea Res., Part I*, *5*(3), 1335–1343, doi:10.1016/j.dsr.2006.06.003.

Primeau, F., and E. Deleersnijder (2009), On the time to tracer equilibrium in the global ocean, *Ocean Sci.*, *5*, 13–28.

Primeau, F., and M. Holzer (2006), The ocean's memory of the atmosphere: Residence-time and ventilation-rate distributions of water masses, *J. Phys. Oceanogr.*, *36*, 1439–1456.

Sarmiento, J., and J. R. Toggweiler (1984), A new model for the role of the oceans in determining atmospheric pCO_2, *Nature*, *308*, 621–624.

Sarmiento, J. L., and N. Gruber (2006), *Ocean Biogeochemical Dynamics*, 503 pp., Princeton Univ. Press, Princeton, N. J.

Sarmiento, J. L., and J. Orr (1991), Three-dimensional simulations of the impact of Southern Ocean nutrient depletion on the atmospheric CO_2 and ocean chemistry, *Limnol. Oceanogr.*, *36*, 1928–1950.

Sarmiento, J. L., N. Gruber, M. A. Brzezinski, and J. P. Dunne (2004), High-latitude controls of thermocline nutrients and low latitude biological productivity, *Nature*, *427*, 56–60.

Schlitzer, R. (2002), Carbon export fluxes in the Southern Ocean: Results from inverse modeling and comparison with satellite based estimates, *Deep-Sea Res. II*, *49*, 1623–1644.

Schlitzer, R. (2004), Export production in the equatorial and north Pacific derived from dissolved oxygen, nutrient and carbon data., *J. Oceanogr.*, *60*, 53–62.

Schlitzer, R., R. Usbeck, and G. Fischer (2004), Inverse modeling of particulate organic carbon fluxes in the south Atlantic, in *The South Atlantic in the Late Quaternary–Reconstructions of Material Budget and Current Systems*, edited by G. Wefer, S. Mulitza, and V. Rathmeyer, pp. 1–19, Springer-Verlag, Berlin.

Siegenthaler, U., and T. Wenk (1984), Rapid atmospheric CO_2 variations and ocean circulation, *Nature*, *308*, 624–625.

Sigman, D., and E. A. Boyle (2000), Glacial/interglacial variations in atmospheric carbon dioxide, *Nature*, *407*, 859–869.

Sigman, D., M. P. Hain, and G. H. Haug (2010), The polar ocean and glacial cycles in atmospheric CO_2 concentration, *Nature*, *446*, 47–55.

Toggweiler, J. R., and B. Samuels (1993), New radiocarbon constraints on the upwelling of abyssal water to the ocean's surface, in *The Global Carbon Cycle, NATO ASI Ser. I, Global Environ. Change*, edited by M. Heinmann, pp. 333–366, Springer, New York.

Trenberth, K. E., J. G. Olson, and W. G. Large (1989), A global ocean wind stress climatology based on ECMWF analyses, *Tech. Rep. TN-338+STR, Natl. Center for Atmos. Res.*, Boulder, Colo.